Structural Analysis of Human and Transgenic Mouse-derived Tau Protein Aggregates

by

Shelaine Fleck

A thesis submitted in partial fulfillment of the requirements for the degree of

Master of Science

Department of Biochemistry
University of Alberta

Abstract

Tauopathies are a class of neurological disorders associated with the aggregation of the tau protein into neurofibrillary tangles. The most prominent tauopathy is Alzheimer's disease (AD), which presents as two forms: early onset (familial, fAD) and late onset (sporadic, sAD). sAD does not have a known cause, although environmental, lifestyle, and genetic factors are thought to contribute to the disease manifestation. fAD can be caused by a single gene mutation in the amyloid precursor protein (APP), presenilin 1, or presenilin 2. In both forms of AD, the tau protein aggregates to form intracellular fibrillary tangles, which spread along neuronal networks. Amyloid-β, the product of APP proteolysis, also contributes to AD through the formation of extracellular amyloid plaques which, according to the amyloid cascade hypothesis, initiates all other associated pathological events, including tau deposition. Together, tau and amyloid-β lead to the extensive neuronal death seen in AD. The structure of tau fibrils in AD, either as Paired Helical Filaments (PHFs) or Straight Filaments (SFs), was solved using cryo-electron microscopy and 3D-reconstructions. By analyzing PHFs and SFs from sAD, researchers found that filament cores consist of two identical protofilaments which adopt a cross-β structure. Later, researchers analyzed additional samples from sAD and fAD cases, which confirmed the initial findings.

Other tauopathies, such as frontotemporal dementia with parkinsonism linked to chromosome 17 (FTDP-17), are caused solely by the misfolding of the tau protein. This disease is characterized by the dementia they cause and notable brain atrophy. The atomic structure of tau fibrils in FTDP-17 is currently unknown.

Through imaging via electron microscopy (EM) and 3D-reconstruction of tau fibrils from both mouse and human sources, we intend to elucidate differences in tau structure which correspond with disease manifestation. There are many different diseases which the tau protein is implicated in. In this project we are focusing on Alzheimer's disease and FTDP-17 using human and mouse brain samples, respectively.

Preface

This thesis is an original work by Shelaine Fleck. The research project, of which this thesis is a part, received ethics approval from the University of Alberta Research Ethics Board, Project Name “Human prions and other misfolded proteins – analyzing the molecular structure of the misfolded conformers”, NO. Pro00042442, Approval expiry date: October 15, 2020.

Some of the research conducted for this thesis forms part of an international research collaboration, led by Dr. Jiri Safar at the Case Western Reserve University, with Dr. Holger Wille and Dr. David Westaway being the lead collaborators at the University of Alberta. The purification for mouse and human samples referred to in chapter 2 was carried out under the supervision of Dr. David Westaway and Dr. Jiri Safar, respectively. The remainder of the techniques in chapter 2, the data analysis carried out in chapters 3 and 4, and the concluding analysis in chapter 5 and 6 are my original work, as well as the literature review in chapter 1.

Acknowledgements

There are many people who I would like to thank for helping and supporting me throughout my Masters' degree.

Firstly, to Dr. Holger Wille, my supervisor. Without his guidance and support this project would not be what it is today. Secondly, to Andrew Fang, my partner and lab-mate. His unconditional support and advice helped me through some of the biggest struggles I have faced during this project.

I would also like to thank all of the collaborators for this project: Ghazaleh Eskandari-Sedighi for her work with the mouse samples; Razieh Kamali-Jamil for starting work on this project before I came to the lab and for allowing me to use the data she collected; Dr. Jiri Safar, Chae Kim, and Dr. Miroslava Kacirova for their work with the human samples; and our past and present microscope technicians, respectively, Dr. Xiongyao Wang and Dr. YongLiang Wang, for their expertise.

Finally, I would like to thank my family and friends. Their support, even when they don't understand what I am talking about, means everything to me.

Table of Contents

1 Introduction 1

1.1 Tau Protein in Cells 1

1.1.1 Post-translational Modifications 4

1.1.2 Cellular Structure of the Tau Protein 7

1.1.3 Tau Protein Interactions 8

1.1.4 Tau Localization in the Brain 9

1.2 Tauopathies 9

1.2.1 Alzheimer's Disease 11

1.2.2 Frontotemporal Dementia and Parkinsonism Linked to Chromosome 17 15

1.3 Tau Protein in Disease 16

1.3.1 Tau Structures 17

1.4 Electron Microscopy 26

1.4.1 Basics of the Transmission Electron Microscope 26

1.4.2 Image Processing for Electron Microscopy 29

1.5 Aims and Hypothesis of the Thesis Project 29

2 Materials and Methods 31

2.1 Tau Protein Purification from Mouse Brain 31

2.2 Tau Protein Purification from Human Brain 32

2.3 Negative Stain Electron Microscopy 32

2.4 3D-reconstruction 33

2.5 Cross-section Rotation 33

3 Structural Analysis of Mouse-derived Tau Protein Aggregates 36

3.1 Characterization of Mouse-derived Tau Protein Aggregates 36

3.1.1 Electron Microscopic Characterization of Mouse-derived Tau Protein Aggregates 40

3.1.2 3D-reconstruction and measurements of Mouse-derived Tau Protein Aggregates 42

4 Structural Analysis of Human-derived Tau Protein Aggregates 46

4.1 Characterization of Human-derived Tau Protein Aggregates 46

4.1.1 Electron Microscopic Characterization of Human-derived Tau Protein Aggregates 48

4.1.2 3D-reconstruction and measurements of Human-derived Tau Protein Aggregates 50

5 Discussion 53

5.1 Structural Comparison of Mouse-derived Tau Filaments and Relevance to Disease 53

5.2 Structural Comparison of Human-derived Tau Filaments and Relevance to Disease 58

5.3 Comparison of Mouse and Human-derived Tau Filaments 62

6 Conclusion 64

7 References 64

List of Figures

1.1 Tau protein domains and alternative splicing in the human CNS 3
1.2 Map of tau post-translational modifications 5
1.3 Diagram representing the influence of phosphorylation on tau microtubule binding 7
1.4 Cellular tau protein structures 7
1.5 Stages I-VI of tau neurofibrillary pathology 15
1.6 Schematic representation of the MAPT gene with FTDP-17 causing mutations 15
1.7 Atomic structures of VQIINK and VQIVKY steric zippers 17
1.8 Ribbon diagrams of AD PHF and SF tau filament folds. 19
1.9 Ribbon diagrams of Pick's disease tau filament folds. 21
1.10 Ribbon diagrams of CTE type I and type II tau filaments. 23
1.11 Ribbon diagrams of CTE type I and type II tau filament folds. 25
1.12 Transmission electron microscope schematic 28
2.1 Overview of the 3D-reconstruction process 35
3.1 The five mouse pathology classes 38
3.2 Electron micrographs of mouse-derived tau fibrils 39
3.3 Electron micrographs of tau fibrils from class III samples 40
3.4 3D-reconstructions of fibrils from mouse pathology classes I-IV 41
4.1 Levels and conformational characteristics of sarkosyl-insoluble tau in sAD and fAD 47
4.2 Electron micrographs of PHFs and SFs from rpAD and spAD cases 49
4.3 3D-reconstruction of PHFs from rpAD and spAD 51
5.1 Electron micrographs of tau filaments from FTDP-17 with a P301L mutation . 55
5.2 Top view and side-by-side comparison of tau PHF 3D-reconstructions with published structure 59
5.3 Comparison of tau filament cores from CDB, PiD, AD, and CTE 63

List of Tables

1.1 Classification of tauopathies according to predominant tau isoform 11
3.1 Distribution of tau fibril morphologies in pathology class III 41
3.2 Distribution of tau fibril morphologies according to pathology class 41
3.3 Width and helical pitch measurements of tau fibrils from pathology classes I-IV 45
4.1 Fibril counts of PHF and SF in rpAD and spAD cases 50
4.2 Width and helical pitch measurements of PHFs and SFs from rpAD and spAD cases 52

Abbreviations

AD	Alzheimer's Disease
Aβ	Amyloid-β
APP	Amyloid precursor protein
ApoE	Apolipoprotein E
AGD	Argyrophilic grain disease
CNS	Central nervous system
CCD	Charge-coupled device
CTE	Chronic traumatic encephalopathy
CMOS	Complementary metal-oxide semiconductor
CDI	Conformation-dependent immunoassay
CSA	Conformational stability assay
CBD	Corticobasal degeneration
DDD	Direct detection device
EM	Electron microscopy/microscope
fAD	Familial Alzheimer's disease
FEG	Field-emission gun
FTDP-17	Fronto-temporal dementia and parkinsonism linked to chromosome 17
GGT	Globular glial tauopathy
MAPT	Microtubule associated protein tau
MTBD	Microtubule binding domain
MW	Molecular weight
NFT	Neurofibrillary tangle
NPF	Narrow Pick filament
PHF	Paired helical filament
PiD	Pick's disease
PSP	Progressive supranuclear palsy
PRD	Proline rich domain
rpAD	Rapidly progressive Alzheimer's disease
SEM	Scanning electron microscope
sAD	Sporadic Alzheimer's disease
SH3	Src homology-3
SF	Straight filament
spAD	Slowly progressive Alzheimer's disease
TEM	Transmission electron microscope/microscopy
UA	Uranyl acetate
WPF	Wide Pick filament

Chapter 1

Introduction

1.1 Tau protein in cells

The microtubule-associated protein tau (tau protein) is a microtubule binding protein encoded by the microtubule associated protein tau (MAPT) gene, located on chromosome 17 in humans (Guo *et al.*, 2017). The MAPT gene is comprised of 134kb (Caillet-Boudin *et al.*, 2015), corresponding to 352-441 amino acids (depending on isoform) (Guo *et al.*, 2017). There are four main regions of tau: the N-terminal region corresponding to exons 1-3 (Guo *et al.*, 2017), the proline rich domain (PRD) corresponding to exons 4-8 (Mandelkow *et al.*, 2012), the microtubule binding domain (MTBD) corresponding to exons 9-12 (Guo *et al.*, 2017), and the C-terminal region corresponding to exon 13 (Guo *et al.*, 2017). After transcription, the MAPT gene undergoes alternative splicing to produce 6 isoforms of the tau protein (Guo *et al.*, 2017) (Figure 1.1). Exon 10, one of the microtubule binding repeats, is alternatively spliced to yield 3R (containing 3 microtubule binding repeats) or 4R (containing 4 microtubule binding repeats) tau (Goedert *et al.*, 1989b), and exons 2 and 3, N-terminal inserts, are alternatively spliced to yield 0N (containing 0 N-terminal inserts), 1N (containing 1 N-terminal insert), and 2N

(containing 2 N-terminal inserts) tau (Goedert *et al.*, 1989a). These isoforms vary in their microtubule binding strength along with location and level of expression. 4R tau isoforms have greater microtubule binding capacity than 3R tau isoforms, as they contain an addition microtubule binding region (Noble *et al.*, 1989). 2N tau isoforms are less abundant then 0N or 1N isoforms, while 3R and 4R tau isoforms are present in relatively equal amounts (Goedert *et al.*, 1989b). Tau is preferentially found in neurons in the central nervous system (CNS) (Guo *et al.*, 2017), although it can also be found in astrocytes (Papasozomenos *et al.*, 1987) and oligodendrocytes (Muller *et al.*, 1997) at lower levels.

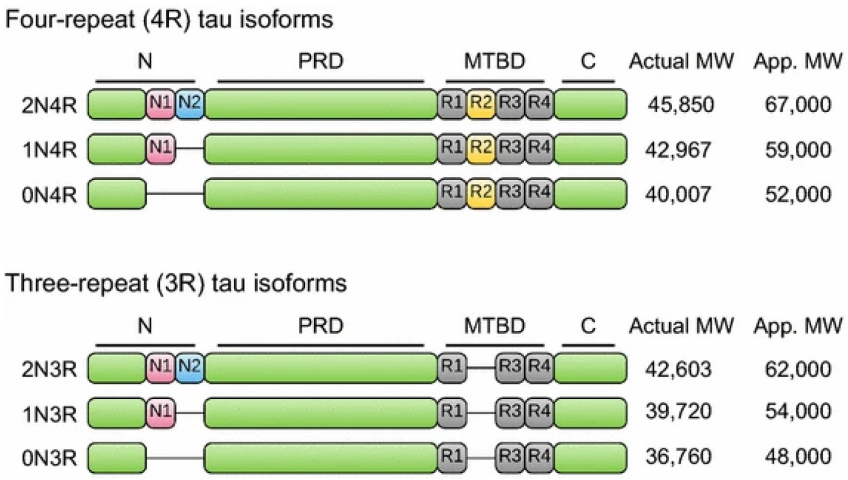

Figure 1.1. Tau protein domains and alternative splicing in the human CNS. Six tau isoforms are generated from the alternative splicing of the MAPT gene. The N-terminal domain contains exons 2 and 3 which are differentially included or excluded to give rise to 2N (exons 2 and 3), 1N (exon 2), and 0N tau isoforms. The PRD is found in the central region of tau, comprised of exons 4-8, is common to all tau isoforms. Exons 9-12 make up the MTBD. Inclusion or exclusion of exon 10 in this domain gives rise to 4R and 3R tau isoforms, respectively. The C-terminal region of tau consists of exon 13 and is common to all tau isoforms. The actual and apparent molecular weight (MW) in kDa is listed for each tau isoform on the right. This figure was reproduced with permission under the Creative Commons license (http://creativecommons.org/licenses/by/4.0/) from Guo *et al.* (2017).

1.1.1 Post translational modifications

Tau can undergo numerous post-translational modifications including phosphorylation, isomerization, glycation, nitration, addition of β-linked N-acetylglucosamine, acetylation, oxidation, polyamination, sumoylation, and ubiquitylation (Guo *et al.*, 2017) (Figure 1.2). The most common of these modifications is phosphorylation and it will be the primary focus here. The tau protein contains 85 phosphorylation sites (Hanger *et al.*, 2009). Tau phosphorylation reduces its affinity for microtubules, resulting in neuronal cytoskeleton destabilization (Guo *et al.*, 2017). Specifically, phosphorylation at Ser262, Ser293, Ser324, and Ser356, located within the microtubule binding repeats, decreases tau binding to microtubules (Drewes *et al.*, 1995) (Figure 1.3). Additionally, phosphorylation at Thr214, Thr231, and Ser325 contribute to dissociation from microtubules (Ksiezak-Reding *et al.*, 2003, Sengupta *et al.*, 1998). Phosphorylation of the tau protein is also linked to increased aggregation, although it is unclear whether phosphorylation occurs before or after aggregation begins (Kopke *et al.*, 1993). For the purpose of this thesis we will assume phosphorylation occurs first. Once tau has been released from the microtubules by phosphorylation, it can self-aggregate to form oligomers and other higher order structures which are linked to disease. The extent by which phosphorylation increases the rate of tau aggregation depends on the region of the protein that is phosphorylated. Phosphorylation in the proline rich region induces a subtle increase in aggregation ability (Eidenmuller *et al.*, 2001), whereas phosphorylation in the C-terminal region markedly promotes tau aggregation (Liu *et al.*, 2007). In addition to disrupting microtubule binding, phosphorylation of the tau protein can also induce tau mis-sorting (Hoover *et al.*, 2010), disrupt the route of degradation (Guo *et al.*, 2017), and alter the association of tau with its binding partners (Hanger *et al.*, 2009).

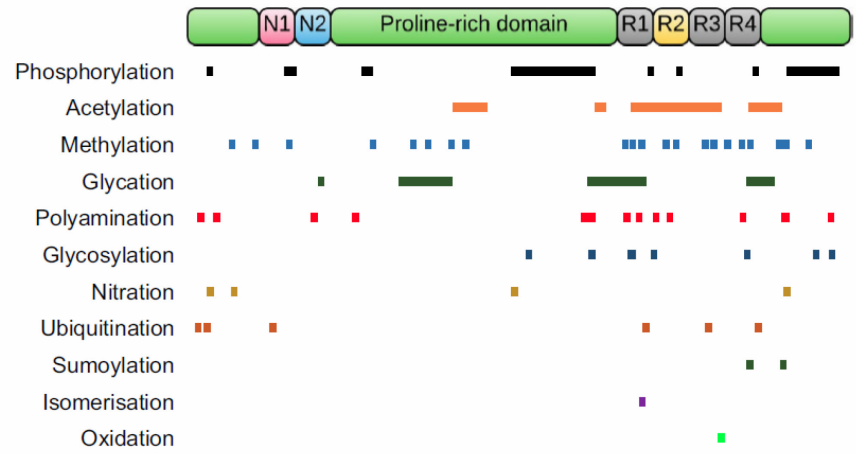

Figure 1.2. Map of tau post-translational modifications. The colored bars indicate the approximate location of each modification listed on the 2N4R tau isoform (441 amino acids). This figure was reproduced with permission under the Creative Commons license (http://creativecommons.org/licenses/by/4.0/) from Guo *et al.* (2017).

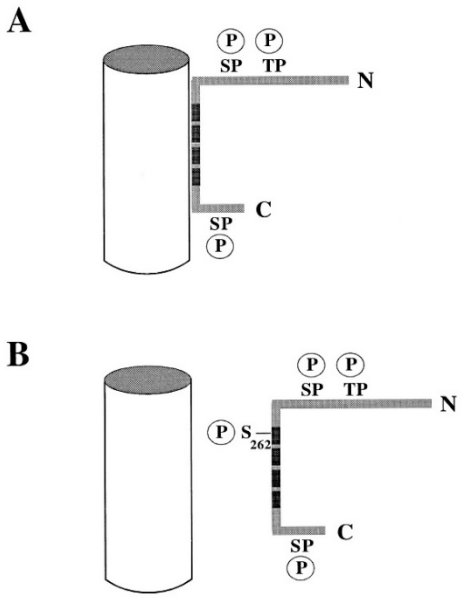

Figure 1.3. Diagram representing the influence of phosphorylation on tau microtubule binding. A. The tau protein binds to a microtubule using the MTBD and can be phosphorylated in regions outside the MTBD. **B.** The MTBD of tau is phosphorylated at Ser 262 which impacts the ability of tau to bind microtubules by reducing its affinity and therefore decreasing microtubule binding. This figure was reproduced with permission of American Soc for Biochemistry & Molecular Biology from Microtubule-associated Protein/Microtubule Affinity-regulating Kinase (p110mark) A NOVEL PROTEIN KINASE THAT REGULATES TAU-MICROTUBULE INTERACTIONS AND DYNAMIC INSTABILITY BY PHOSPHORYLATION AT THE ALZHEIMER-SPECIFIC SITE SERINE 262, Drewes *et al.* 1995; permission conveyed through Copyright Clearance Center, Inc.

1.1.2 Cellular structure of the tau protein

The tau protein is widely accepted to be a natively unfolded protein that does not have significant secondary structure (Jeganathan *et al.*, 2008). This allows tau to maintain a flexible conformation which can adapt to form different intramolecular interactions between its charged domains. One proposed conformation for free, cytoplasmic tau isoforms is a 'paperclip'. In this conformation the C-terminus folds over the microtubule binding domain and the N-terminus folds back over the C-terminus (Jeganathan *et al.*, 2006). This brings the N- and C-termini into close proximity. In order to interact with microtubules, the tau protein must adopt a different structure. The N- and C-termini 'open' to expose the microtubule binding domain allowing it to interact with the microtubule (Jeganathan *et al.*, 2008). The N-terminus is now projected away from the microtubule where it can regulate microtubule dynamics (Chen *et al.*, 1992). The C-terminus does not have any known interactions upon adoption of the 'open' tau structure (Guo *et al.*, 2017).

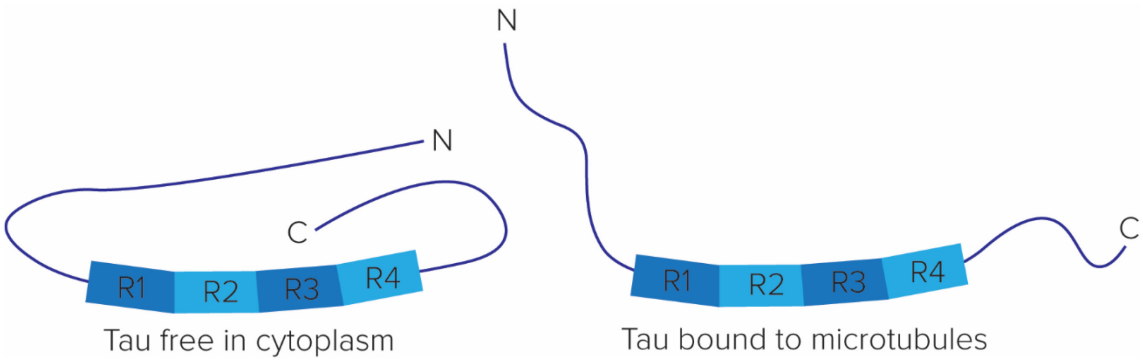

Figure 1.4. Cellular tau protein structures. The tau protein adopts a 'paperclip' conformation when free in the cytoplasm. The N- and C- termini fold over towards each other and the MTBD. When tau binds to microtubules this 'paperclip' opens to allow the MTBD to interact with the microtubule. The N-terminus projects away from the microtubule.

1.1.3 Tau protein interactions

The tau protein can interact with numerous proteins in the cell via its N-terminus, proline rich domain, and microtubule binding repeats. The N-terminal inserts have few specific, known interactions; however, they may influence the distribution and localization of the tau protein (Guo *et al.*, 2017). Isoforms 0N, 1N, and 2N show different localization patterns (Liu *et al.*, 2013b). The N-terminus may also interact with protein annexin A2 (Brandt *et al.*, 1995) - a membrane binding protein - and the p150 subunit of the dynactin complex (Magnani *et al.*, 2007), which mediates dynein association with microtubules. Finally, there are some proteins which interact only with certain N-terminal inserts. An example of this is apolipoprotein A1, which preferentially binds 2N tau isoforms (Liu *et al.*, 2016).

The proline rich domain of the tau protein contains potential recognition sites for Src homology-3 (SH3) proteins through its PXXP motif. The SH3 group contains proteins such as the protein kinases Lck (Lee *et al.*, 1998), Fgr (Reynolds *et al.*, 2008), and Fyn (Lee *et al.*, 1998); the regulatory subunit of phosphatidylinositol 3-kinase; phospholipase C (Jenkins *et al.*, 1998); and others. The interactions of the proline rich domain with SH3 containing proteins likely have roles in regulation of the signaling functions of tau (Guo *et al.*, 2017). The proline rich domain also has a DNA (Qi *et al.*, 2015) or RNA (Wang *et al.*, 2006) interacting site, which may assist in the localization of tau to the nucleus (Bukar Maina *et al.*, 2016). Lastly, there is evidence of the proline rich domain assisting in regulating microtubule assembly (Goode *et al.*, 1997) and actin binding (He *et al.*, 2009).

The microtubule binding repeats of the tau protein mediate its interactions with microtubules (Mukrasch *et al.*, 2007). The four repeats are imperfect, meaning they do not have the same amino acid sequences (Lee *et al.*, 1988). This difference accounts for the varied affinities for microtubules these repeats have (Noble *et al.*, 1989). The microtubule binding domains are responsible for enabling the binding of the actin to

microtubules (Correas *et al.*, 1990). At least two microtubule binding domains are needed to link actin to the microtubule, tethering them together (Elie *et al.*, 2015).

1.1.4 Tau localization in the brain

In the human brain, under physiological conditions the tau protein is expressed in neurons (Guo *et al.*, 2017), oligodendrocytes (Muller *et al.*, 1997), and astrocytes (Papasozomenos *et al.*, 1987). In neurons, tau is primarily located in the axon (Trojanowski *et al.*, 1989), although it can also be found in the plasma membrane (Tashiro *et al.*, 1997), nucleus (Tashiro *et al.*, 1997), and mitochondria (Li *et al.*, 2016). Tau mRNA is targeted to the axonal compartment by the axonal localization signal site in the 3'-untranslated region of the MAPT gene (Aronov *et al.*, 2001). It can also be transported to the axons from the cytosol by motor proteins or by diffusing freely (Konzack *et al.*, 2007). The tau protein is retained at the axon by maintaining low phosphorylation levels and by a retrograde barrier formed by the axon which allows tau to enter but prevents it from leaving (Li *et al.*, 2011).

The tau protein can also be found in dendrites, albeit at significantly lower levels (Guo *et al.*, 2017). The role of tau here is not well understood; however, it has been implicated in the regulation of hippocampal plasticity (Chen *et al.*, 2012) along with the formation, size, and trafficking of stress granules (Vanderweyde *et al.*, 2016).

1.2 Tauopathies

Tauopathies refers to a group of dementias and movement disorders that are characterized by intracellular accumulations of tau filaments that form neurofibrillary tangles in neurons and glial cells. They are further classified into primary and secondary tauopathies, depending on whether the tau protein is the major contributing factor or associated with other pathologies (Arendt *et al.*, 2016). Primary tauopathies include Pick's

disease (PiD), progressive supranuclear palsy (PSP), corticobasal degeneration (CDB), argyrophilic grain disease (AGD), sporadic multiple system tauopathy with dementia, frontotemporal dementia with parkinsonism linked to chromosome 17 (FTDP-17), and globular glial tauopathy (GGT) (Kovacs, 2016). These primary tauopathies can then be even further classified into sporadic or familial occurrence (Arendt *et al.*, 2016). Most of the diseases listed above do not have any associated genetic mutations and are therefore considered to be a sporadic disease (Arendt *et al.*, 2016). The exception to this is FTDP-17 which is typically due to mutations in the MAPT gene (Hutton *et al.*, 1998). Secondary tauopathies include Alzheimer's disease (AD), chronic traumatic encephalopathy (CTE), some prion diseases, and Huntington's disease (Arendt *et al.*, 2016). In these diseases, tau pathology occurs with other types of pathology. Like primary tauopathies, these diseases can be sporadic or familial in nature (Arendt *et al.*, 2016).

Tauopathies can be further classified by their tau isoform pattern. Based on the ratio of 3R and 4R isoforms in the neurofibrillary lesions there are four classes of tauopathies (Kovacs, 2016). Class I tauopathies are characterized by the presence of all six tau isoforms with approximately equal amounts of 3R and 4R tau (Arendt *et al.*, 2016). This group includes AD and CTE. Class II tauopathies predominantly contain 4R tau isoforms; this group includes PSP, CBD, AGD, and GGT (Arendt *et al.*, 2016). Class III tauopathies predominately contain 3R tau isoforms; this group includes Pick's disease and some FTDP-17 cases (Arendt *et al.*, 2016). The final class, Class IV, consists of tau isoforms lacking exons 2, 3, and 10 (0N3R) and includes myotonic dystrophy (Arendt *et al.*, 2016) (Table 1.1).

Table 1.1. Classification of tauopathies according to predominant tau isoform.

Class I	Class II
3R & 4R tau isoforms	**4R tau isoforms**
Alzheimer's disease Chronic traumatic encephalopathy Some FTDP-17 cases	Progressive supranuclear palsy Corticobasal degeneration Argyrophilic grain disease Globular glial tauopathy
Class III	**Class IV**
3R tau isoforms	**0N3R tau isoform**
Pick's disease Some FTDP-17 cases	Myotonic dystrophy

1.2.1 Alzheimer's disease

Alzheimer's disease is the most common form of dementia to affect our population. It is characterized by the accumulation of both tau and amyloid-β (Aβ) in the brain. According to the amyloid cascade hypothesis, the aggregation and deposition of Aβ is the starting point of AD development (Hardy *et al.*, 1992). Aβ aggregates and accumulates extracellularly outside the neurons to form plaques (Duyckaerts *et al.*, 2009). This triggers tau to aggregate and accumulate intracellularly in the neuron cell body to form neurofibrillary tangles (NFTs) (Duyckaerts *et al.*, 2009). Together, Aβ and tau lead to neuronal death which results in the shrinking of the brain, particularly the cerebral cortex and hippocampus, and the enlargement of ventricles.

The progression of AD can be determined using the Braak system (Braak *et al.*, 2006). The Braak system describes the development and spreading of pathology in the brain as the disease progresses. In Stage I, lesions develop in the transentorhinal region of the cerebral cortex. In Stage II, lesions extend to the entorhinal region, particularly the superficial cellular layer, and the hippocampus. Stage III lesions extend to the neocortex

of the fusiform and lingual gyrus and lesions in stage II sites become more severe. Stage IV represents the progression of pathology into neocortical association areas of the temporal lobe, not quite reaching the superior temporal gyrus. In stage V, neocortical pathology extends in frontal, superolateral, and occipital directions and reaches the peristriate area and the superior temporal gyris. Stage VI pathology now includes the secondary and primary neocortical areas and extends to the striate area of the occipital lobe. At this point pathology can be seen throughout the brain (Figure 1.5).

AD has both a sporadic and a familial form of disease. Sporadic AD (sAD), also known as late onset AD, does not have a known cause, although environmental, lifestyle, and genetic factors may have a role in the development of disease (Liu *et al.*, 2013a). sAD can be further classified into slowly progressive (spAD) and rapidly progressive (rpAD) depending on the time taken for the disease to progress. The main genetic determinant of sAD is a person's apolipoprotein E (ApoE) allele (Corder *et al.*, 1993). ApoE is a major cholesterol carrier that supports injury repair in the brain and lipid transport (Mahley *et al.*, 2000). There are three alleles of this protein. The most common allele, $\varepsilon 3$, does not increase nor decrease the risk of developing AD (Farrer *et al.*, 1997). Carriers of the $\varepsilon 4$ allele have an increased risk of developing AD (Harold *et al.*, 2009), while carriers of the $\varepsilon 2$ allele have a decreased risk (Farrer *et al.*, 1997). The different isoforms have different abilities to bind lipids, receptors, and $A\beta$. This results in a differential effect on $A\beta$ clearance and aggregation which may contribute to or prevent disease (Liu *et al.*, 2013a). Familial AD (fAD), also known as early onset AD, is caused by genetic mutations on chromosomes 14 (Thinakaran, 1999), 21 (Goate *et al.*, 1991), or 1 (Thinakaran, 1999). Each of these single gene mutations results in abnormal cleavage of the amyloid precursor protein (APP), leading to the formation of abnormal $A\beta$. A mutation on chromosome 14 directly results in abnormal APP. Mutations on chromosomes 21 and 1 both alter the presenilin protein (Thinakaran, 1999, Tomita *et al.*, 1997), which is responsible for the

cleavage of the APP; a mutation of chromosome 21 results in abnormal presenilin 1 protein (Kelleher *et al.*, 2017); and mutation on chromosome 1 results in abnormal presenilin 2 protein (Tomita *et al.*, 1997). Both mutations will result in abnormal cleavage of the APP to Aβ. The abnormal Aβ protein generated in these cases is more likely to aggregate, and therefore more likely to lead to AD (Erez *et al.*, 2009).

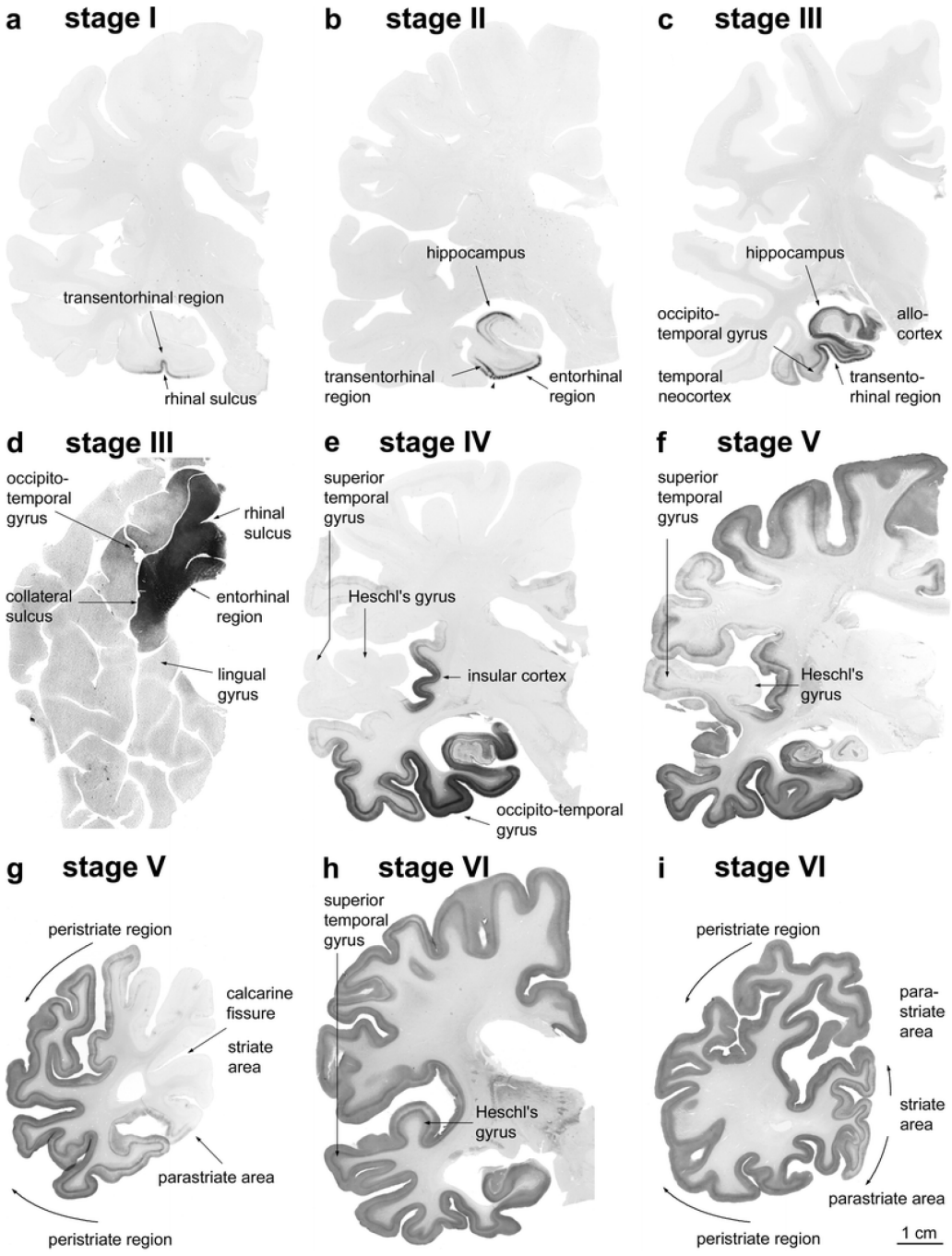

Figure 1.5. Stages I-VI of tau neurofibrillary pathology. 100um polyethylene glycol embedded hemisphere sections were immunostained for hyperphosphorylated tau. Slices show primary areas of tau pathology at each stage. This figure was reproduced with permission under the Creative Commons license (http://creativecommons.org/licenses/by/4.0/) from Braak *et al.* (2006).

1.2.2 FTDP-17

Frontotemporal dementia and parkinsonism linked to chromosome 17 (FTDP-17) is a rare autosomal dominant neurodegenerative disorder (Wszolek *et al.*, 2006). It is characterized by three major features: behavioral disturbance, cognitive impairment, and motor symptoms, or Parkinsonism (Wszolek *et al.*, 2006). FTDP-17 is caused by mutations in the MAPT gene, with over 50 unique mutations identified in 150 families with FTDP-17 (Ghetti *et al.*, 2015) (Figure 1.6). The most common mutations leading to FTDP-17 are P301L, N279K, and exon 10 splice site mutations (Ghetti *et al.*, 2015). The disease-causing mutations can act in two ways. The first is by altering the proportion of tau 3R to 4R isoforms, and the second is by altering the ability of the tau protein to bind to microtubules, thereby increasing tau aggregation leading to filament formation (Wszolek *et al.*, 2006). Once aggregated, the tau protein deposits in neurons or neurons and glia (Ghetti *et al.*, 2015).

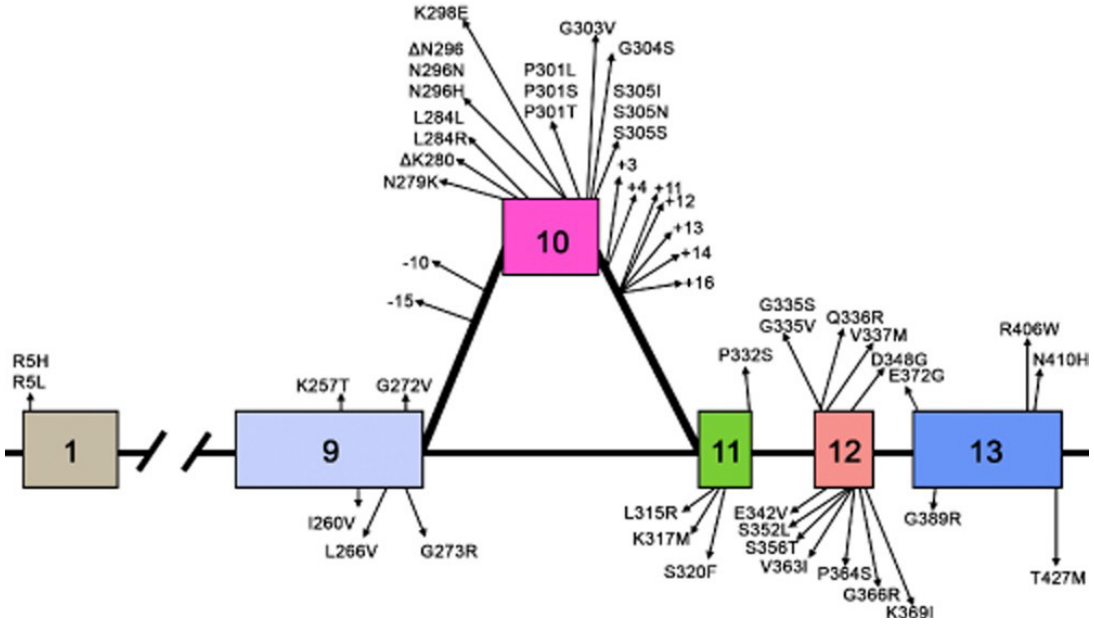

Figure 1.6. Schematic representation of the MAPT gene with FTDP-17 causing mutations. This figure was adapted and reproduced with permission under the Creative Commons Attribution License from Ghetti *et al.* (2015).

Little is known about the early neuropathologic stages of FTDP-17 (Ghetti *et al.*, 2015). In the intermediate stages, cerebral hemisphere atrophy is mild. There may be atrophy of the caudate nucleus and reduction in pigmentation of the substantia nigra and the locus coeruleus. In the advanced stages of disease, atrophy is present throughout the frontal and temporal lobes, caudate nucleus, putamen, globus pallidus, amygdala, hippocampus, and hypothalamus. The superior, middle, and inferior frontal and temporal gyri often are the most affected by the disease. The brain atrophy may involve the frontal and temporal lobes asymmetrically. The parietal and occipital lobes are not frequently affected. There have been some attempts to link MAPT mutations with the path of brain atrophy. Preliminary results have shown that MAPT mutations affecting the splicing of exon 10 are associated with medial temporal lobe involvement (Ghetti *et al.*, 2015). These studies are difficult, however, because of the different rates of atrophy and sequence of anatomical involvement are highly variable, even in cases with the same mutation.

1.3 Tau protein in disease

The tau protein contributes to tauopathy pathogenesis through misfolding and oligomerization into insoluble amyloid deposits. It is these aggregates that affect cell function and lead to neuronal death. The mechanism of formation of these aggregates is not known, although there are some clues within the motifs of tau. There are two hexapeptide motifs location in the second and third MTBD that have high β-sheet propensity (Seidler *et al.*, 2018). These motifs consist of residues 306-311, VQIVKY, and 317-335, VQIINK. These regions of tau will self-assemble into 'steric zippers' and can form fibrillar aggregates *in vitro (S*eidler *et al*., 2018*)* (Figure 1.7). The interaction of these 'steric zipper' regions between tau monomers may lead to dimerization, and eventually oligomerization. The oligomers then assemble into protomers which adopt a parallel, in

register, cross β-sheet structure. It is these amyloid fibrils that result in neurofibrillary pathology seen in tauopathies (Seidler *et al.*, 2018).

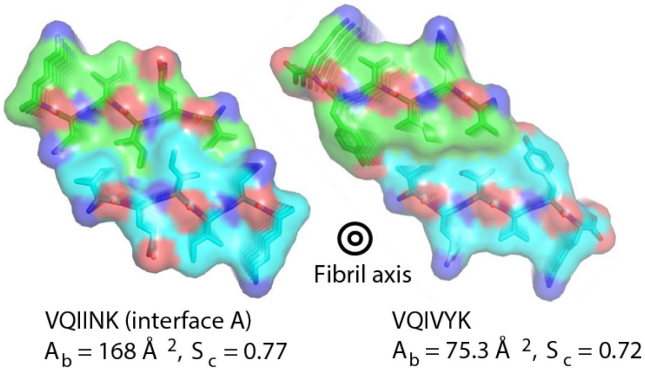

Figure 1.7. Atomic structures of VQIINK and VQIVKY steric zippers. The VQIINK and VQIVYK hexapeptides are found within the tau protein. These motifs will self-assemble into steric zippers, shown here. The strength of these steric zippers is determined by the amount of buried surface area (A_b) and the shape complementarity (S_c). This figure was adapted and reproduced with permission from Springer Nature Customer Service Centre GmbH: Springer Nature, Nature Chemistry, Structure-based inhibitors of tau aggregation, P,M. Seidler *et al.* (2018).

1.3.1 Tau structures

The tau protein has been shown to adopt different structures for different diseases. The structure of the tau protein in AD (Falcon *et al.*, 2018b, Fitzpatrick *et al.*, 2017), PiD (Falcon *et al.*, 2018a), CTE (Falcon *et al.*, 2019), and CBD (Zhang *et al.*, 2020) has been solved using cryo-electron microscopy (cryo-EM). There are some similarities between these structures, but overall, the tau protein adopts a different conformation in each disease. In AD, tau protein inclusions consist of paired helical filaments (PHF) and straight filaments (SF) (Fitzpatrick *et al.*, 2017), containing 3R and 4R tau isoforms, which

each adopt a different structure that is consistent across all cases of AD studied (Falcon *et al.*, 2018b). Both PHFs and SFs are composed of two protofilaments with C-shaped cores which contain 8 β-sheets, coined the cross-β/β-helix C-shaped architecture (Fitzpatrick *et al.*, 2017). This core region contains MTBD repeats 3 and 4. In the protofilament, there is a β-helix-like region consisting of three β-sheets arranged in a triangle and two regions with cross-β architecture. Throughout the protofilament structure there are stabilizing hydrogen bonds along with asparagine and glutamine ladders. Additionally, the hexapeptide $_{306}$VQIVYK$_{311}$, found at the N-terminus of the protofilament, packs in a complementary fashion with residues 373-378 on the opposing β-strand. The difference between PHFs and SFs is at the interface between two protofilaments. The protofilaments make different lateral contacts with each other. In PHFs, the two protofilaments form identical structures related by helical symmetry. The interface is formed by the antiparallel stacking of residues $_{332}$PGGGQ$_{336}$ and stabilized by hydrogen bonds between Q$_{336}$ and K$_{331}$ (Figure 1.8a). In SFs, the two protofilaments pack asymmetrically. The interface is formed by residues $_{321}$KCGS$_{324}$ of the first protofilament and $_{313}$VDLSK$_{317}$ of the second protofilament. However, these residues do not form salt bridges or hydrogen bonds and there is no hydrophobic packing. The SF interface is stabilized by the side chains of K$_{317}$, T$_{319}$, and K$_{321}$ (Figure 1.8b).

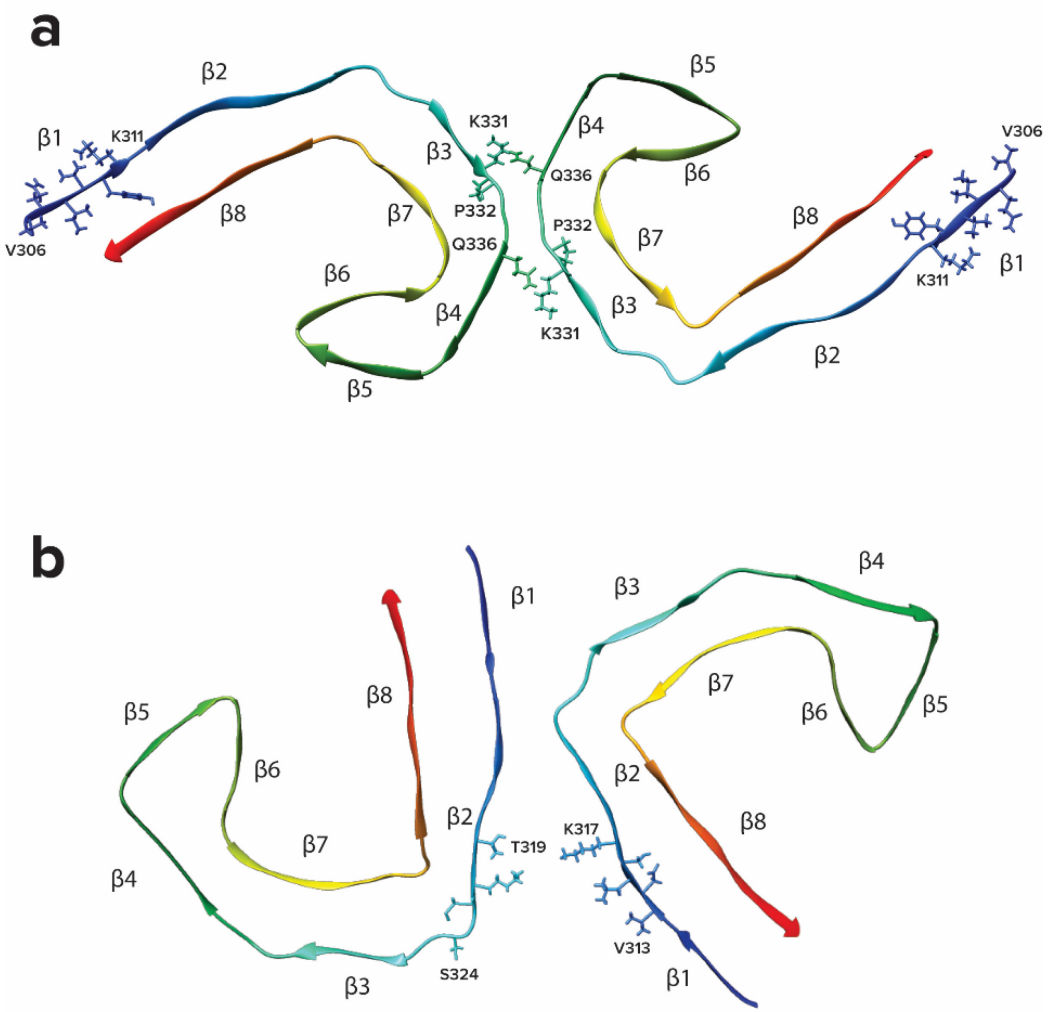

Figure 1.8. Ribbon diagrams of AD PHF and SF tau filament folds. Ribbon diagrams with labelled β-sheets for PHF (a) and SF (b) are shown. **a.** The interface of PHF is formed by two identical protofilament structures related by helical symmetry. Residues P332-Q336 form the interface of PHFs. The steric zipper motif $_{306}$VQIVYK$_{311}$ is shown in β1. **b.** The interface of SF is formed by the asymmetrical packing residues T319-S324 on one protofilament and V313-K317 on the second protofilament (Falcon *et al.*, 2018b, Fitzpatrick *et al.*, 2017).

In PiD, there are narrow and wide Pick filaments (Falcon *et al.*, 2018a) (NPF and WPF, respectively) which contain only 3R tau isoforms. NPFs are composed of a single protofilament with an elongated structure, different from the C-shaped protofilament of AD (Fitzpatrick *et al.*, 2017) (Figure 1.9a). This protofilament contains nine β-strands arranged into four cross-β packing stacks, which are packed together in a hairpin-like fashion: β1 with β8, β2 with β7, β3 with β6, and β4 with β5 (Falcon *et al.*, 2018a). The final β-strand, β9, packs against the opposite side of β8. The cross-β packing interfaces are composed of both polar and non-polar side chains, except for the interface between β3 and β6 which is hydrophobic. WPFs are formed by two NPFs which associate at their distal tips. A hairpin turn between β4 and β5 along with C_{322}, G_{323}, and S_{324} provides the interface for the formation of WPFs (Figure 1.9b). This interaction is stabilized through van der Waals interactions.

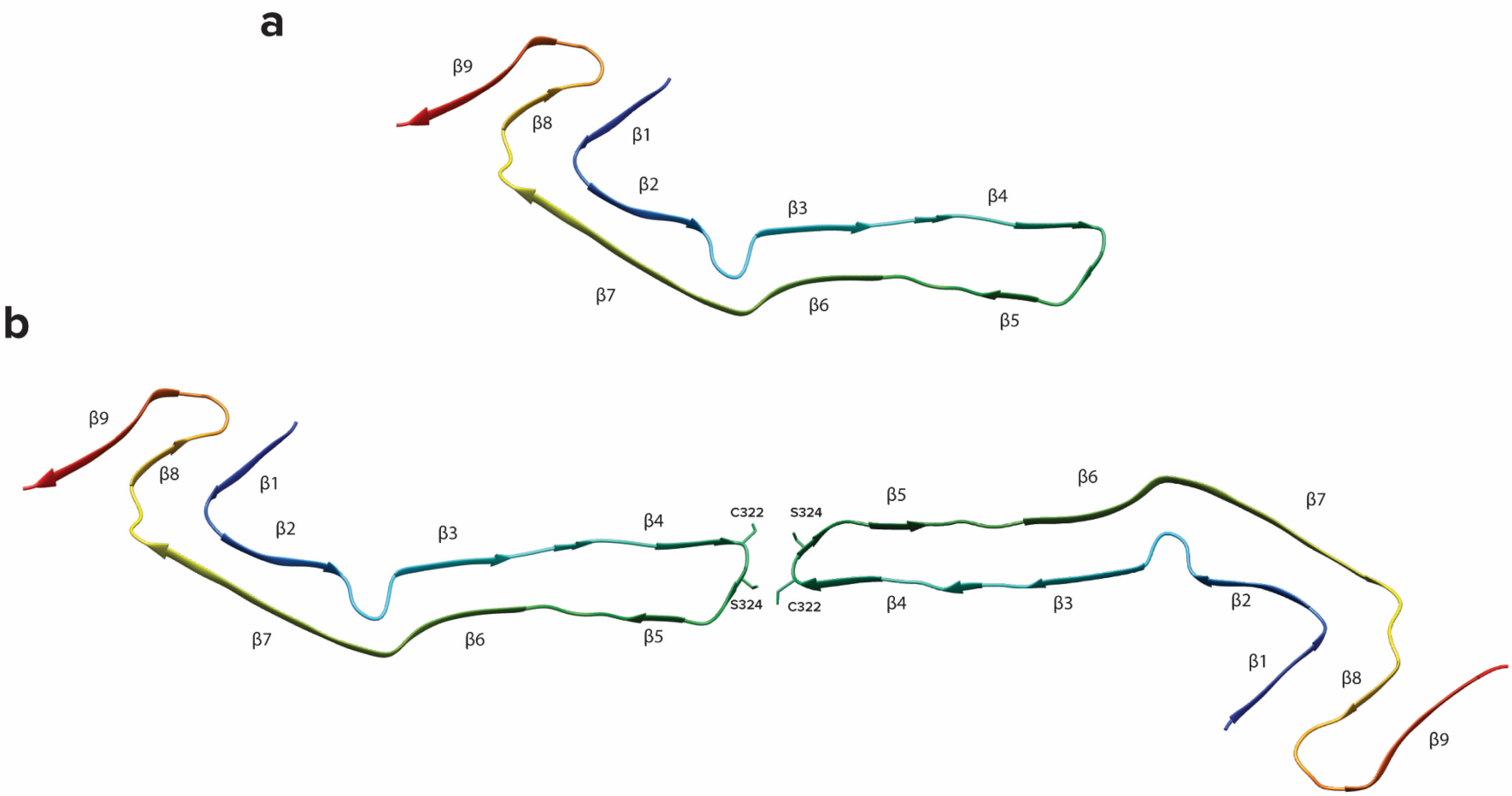

Figure 1.9. Ribbon diagrams of Pick's disease tau filament folds. Ribbon diagrams of NPF (a) and WPF (b) are shown with labelled β sheets. **a.** NPF are composed of a single protofilament. **b.** WPF are formed by the association of to NPF at their distal tips. This interacted is stabilized by C322-S324 on both protofilaments (Falcon *et al.*, 2018a).

In CTE, there are type I and type II tau filaments, which contain all six tau isoforms (Falcon *et al.*, 2019). The protofilament structure is similar to the C-shaped AD fold (Fitzpatrick *et al.*, 2017), but it is more open. Like AD, both type I and type II tau filaments form a cross-β/β-helix fold consisting of 8 β-strands packed against each other: β1 and β2 engage in anti-parallel cross-β packing against β8; β3 packs against β7; and β4-6 form a triangular β-helix that turns the main chain back on itself (Falcon *et al.*, 2019). Additionally, the CTE tau folds contains a hydrophobic cavity within the β-helix motif created by β4, β5, β5 which is suspected to be a non-polar sterol or fatty acid. This molecule is surrounded by the side chains of V339, L344, F346, V350, and I354 and the hydroxyl groups of S341 and S352. Like in AD, type I and type II CTE tau filaments are ultrastructural polymorphs with a common protofilament core but different interfaces. The interface of type I filaments consists of an antiparallel steric zipper formed by $_{324}$SLGNIH$_{329}$ (Figure 1.10a). The interface of type II CTE filaments is formed by the $_{331}$KPGGGQVE$_{338}$ motif (Figure 1.10b). This interface is slightly less stable than the type I interface, which may account for the difference in frequency of these filaments.

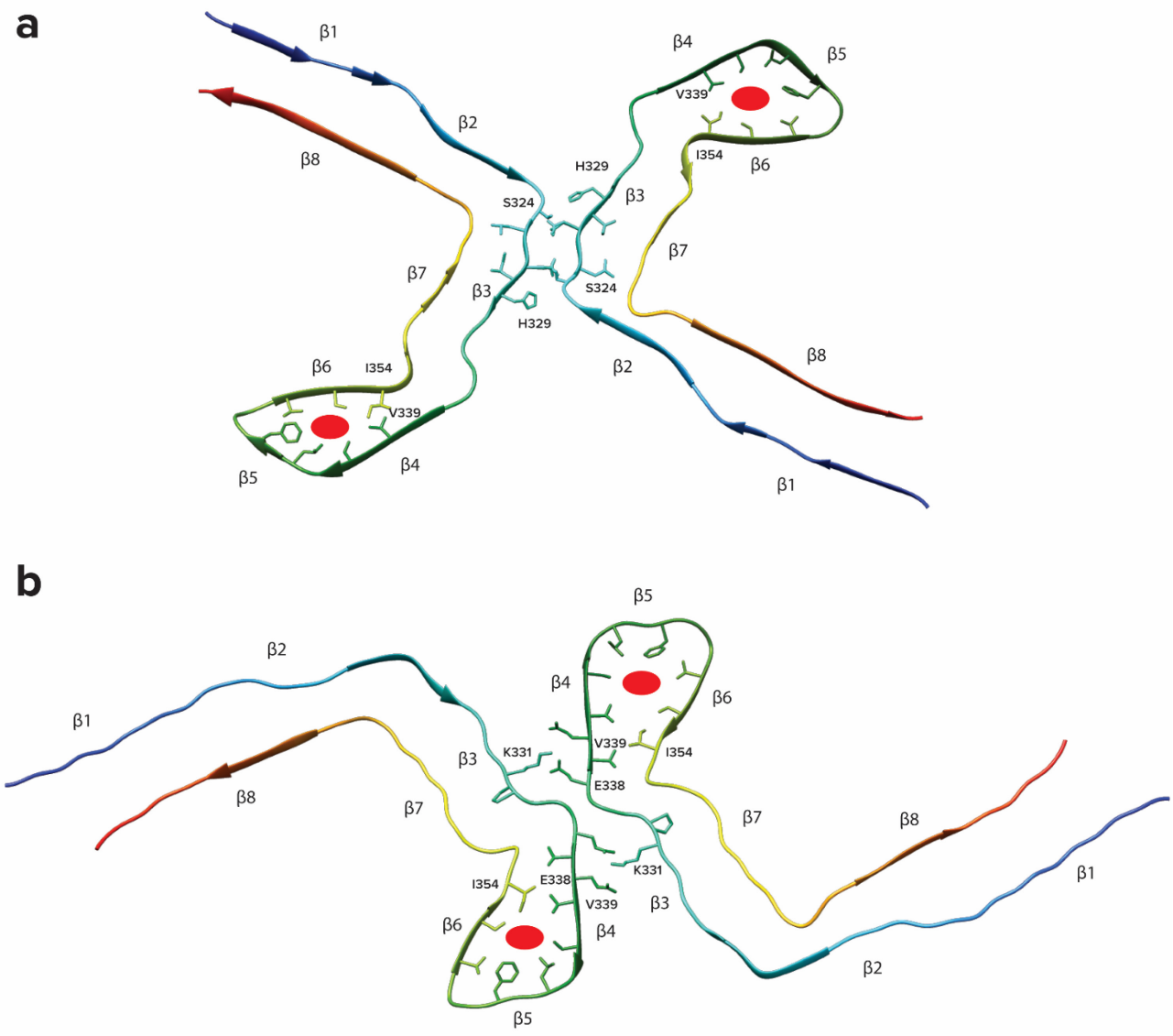

Figure 1.10. Ribbon diagrams of CTE type I and type II tau filaments. Ribbon diagrams of CTE type I (a) and CTE type II (b) folds are shown with labelled β-sheets. **a.** The interface of the type I CTE fold is formed by residues S324-H329. **b.** The interface of the type II CTE fold is formed by residues K331-E338. The hydrophobic cavity is formed by residues V339-I354 in both type I and type II CTE structures and contains a sterol of fatty acid (red circle) (Falcon *et al.*, 2019).

In CBD, there are two tau filament structures, type I (narrow) and type II (wide) (Zhang *et al.*, 2020), a concept which is also seen in PiD fibrils (Falcon *et al.*, 2018a). Type I filaments are composed of a single protofilament; type II filaments contain pairs of identical type I protofilaments related by C2 symmetry (Zhang *et al.*, 2020). Each CBD protofilament contains a region of additional density, suspected to be a polyanionic molecule, surrounded by a positively charged, hydrophilic environment formed by residues K_{290}, K_{294}, and K_{370}. This is similar to the suspected sterol or fatty acid contained in CTE protofilaments (Falcon *et al.*, 2019), which creates a negatively charged, hydrophobic environment. The core structure of the CBD tau fold is formed by residues K274-E380 (Zhang *et al.*, 2020). These residues are organized into 11 β-strands which are connected by turns and arcs to form a four-layered structure. The central four layers are formed by β7, β4, β3, and β10 with strands β3 and β4 connected through a sharp turn and β7 and β10 connected through β8 and β9 which wrap around the turn. On the other side of the core β2, β5, and β6 form a three-layered structure with β2 packed against one end of β5 and β6 against the other end. The remaining β-strands, β1 and β11, pack against each other to close the hydrophilic cavity formed by residues from β2, β3, β10, and β11 (Figure 1.11a). The interfaces between β-strands in the CBD tau fold are composed of a mixture of polar and hydrophobic groups. In type II CBD filaments, the interface between the two protofilaments is formed by anti-parallel stacking of $_{343}$KLDFKDR$_{349}$ (Figure 1.11b) which is stabilized by van der Waals interactions and hydrogen bonds.

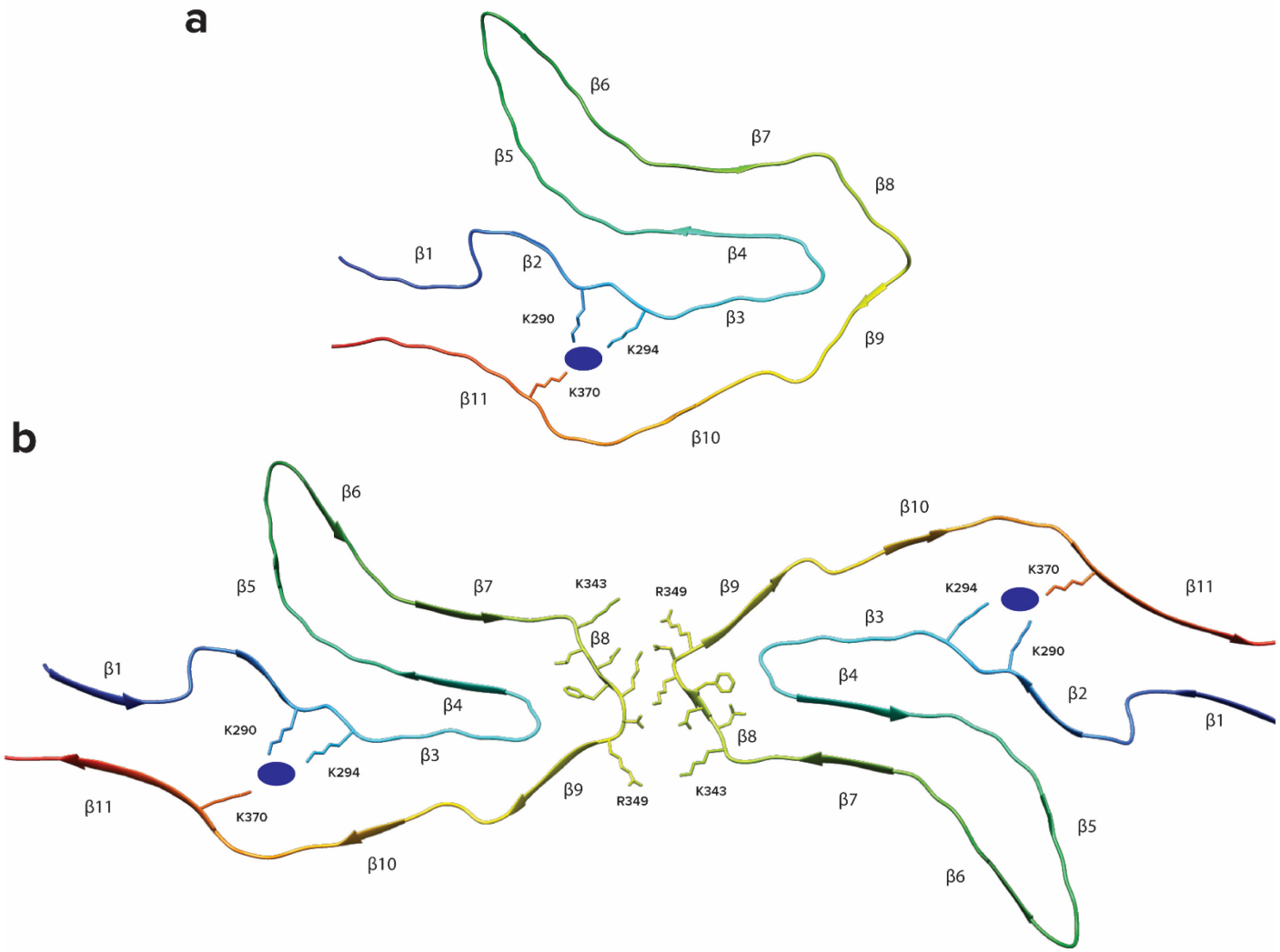

Figure 1.11. Ribbon diagrams of CBD type I and type II tau filament folds. Ribbon diagrams of CBD type I (a) and CBD type II (b) folds are shown with labelled β-sheets. **a.** The type I CBD fold is composed of only one protofilament. **b.** The interface of the type II CBD fold is formed by residues K343-R349. The hydrophilic cavity is formed by residues K290, K294, and K370 in both type I and type II CBD structures and contains a polyanionic molecule (blue circle) (Zhang *et al.*, 2020).

1.4 Electron microscopy

The transmission electron microscope (TEM), constructed for the first time in 1931, has been used in numerous structural biology studies since it first began to gain popularity in the 1940s (Harris, 2015). The other form of electron microscopy, scanning electron microscopy (SEM) is not typically used in the structural biology field and will not be discussed in this thesis. After its development, TEM slowly gained popularity as researchers created better sample preparation techniques; from metal shadowing, to negative staining, and finally to plunge freezing (Harris, 2015). TEM has been used to visualize tissues along with isolated macromolecules and viruses, with the focus shifting to single particle analysis more recently. This shift would not be possible without the advancement of computer technology. This allowed TEM 2D projection images to be transformed into 3D reconstructions using various software packages such as IMAGIC (van Heel *et al.*, 1996), EMAN (Ludtke *et al.*, 1999), and SPIDER (Frank *et al.*, 1996). Today, EM and cryo-EM are extremely popular techniques for studying macromolecules and determining high resolution structural information.

1.4.1 Basics of the transmission electron microscope

The transmission electron microscope uses the same basic principles as a classic light microscope (Williams *et al.*, 1996). However, instead of photons a TEM uses electrons, and instead of a series of glass lenses there is a series of electromagnetic lenses. This allows for the production of images with higher magnification and resolution than what is achievable with a light microscope. Like a light microscope, a TEM can be divided up into three main components: the illumination system, consisting of the electron source and condenser lenses; the objective lens/stage system, where the specimen is inserted; and the imaging system, consisting of lenses to magnify focus the image, and a charge-coupled device (CCD) camera or a direct detection device (DDD) with a

complementary metal-oxide semiconductor (CMOS) camera (Williams *et al.*, 1996) (Figure 1.10). Together, these components allow for the collection of high-resolution images of a sample which can be used to obtain structural information.

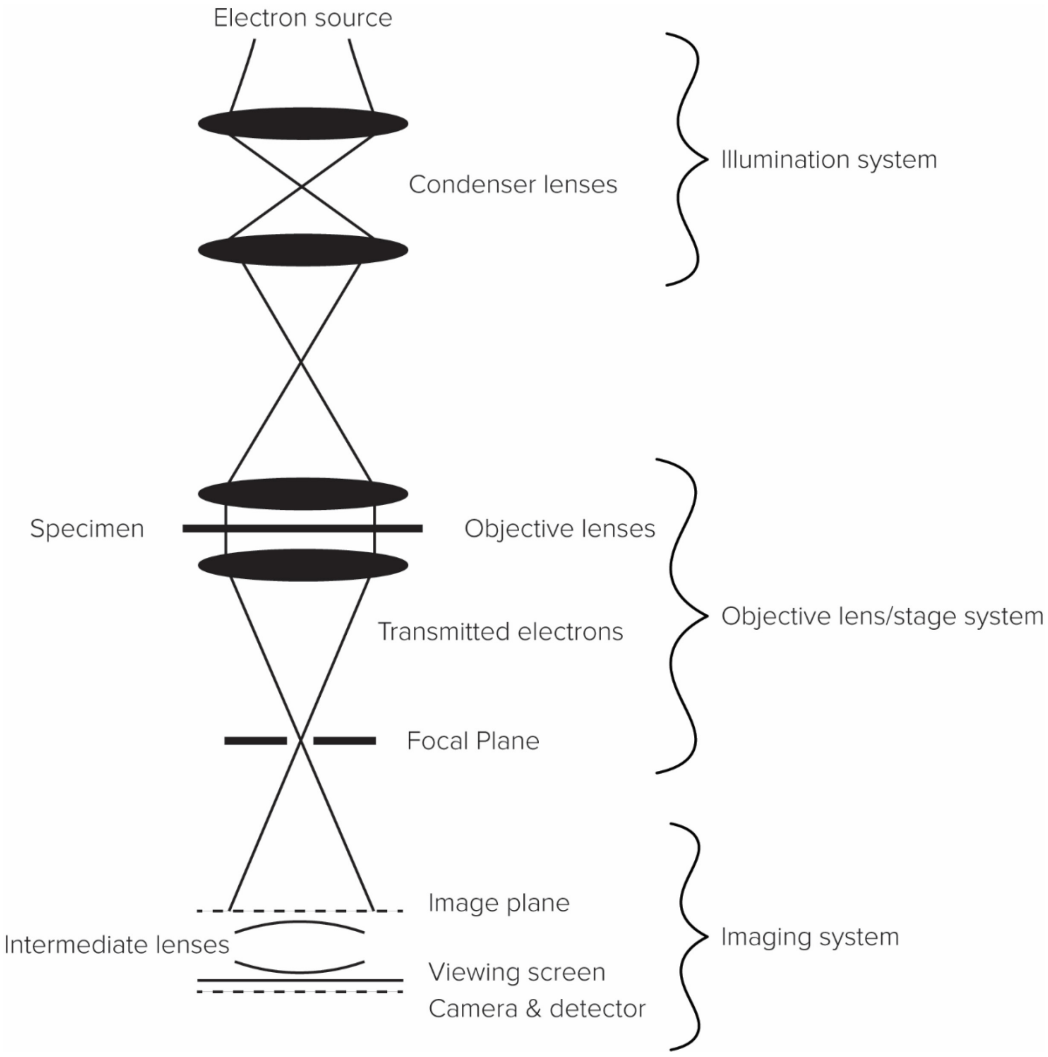

Figure 1.12. Transmission electron microscope schematic. A TEM can be categorized into three major areas: the illumination system, the objective lens/stage system, and the imaging system. The main components of each of these systems are shown. Lines are included to show the path of the electron beam as it passes through various focusing lenses and the sample before reaching a detector.

1.4.2 Image processing for electron microscopy

Electron microscopy would not be what it is today without the numerous programs created for image processing. These programs are used to extract detailed structural information from the raw images collected. Although there are numerous software programs available for use, only EMAN (Ludtke *et al.*, 1999), SPIDER (Frank *et al.*, 1996), IMAGIC (van Heel *et al.*, 1996), and Chimera (Pettersen *et al.*, 2004) will be discussed in this thesis.

1.5 Aims and hypothesis of the thesis project

The tau protein has been shown to be capable of adopting multiple conformations in different diseases, such as AD (Falcon *et al.*, 2018b, Fitzpatrick *et al.*, 2017), CTE (Falcon *et al.*, 2019), PiD (Falcon *et al.*, 2018a), and CBD (Zhang *et al.*, 2020). It is becoming increasingly clear that these so called 'strains' are disease dependent and likely can be attributed to some of the differences seen between tauopathies. While the structures of tau PHFs and SFs in Alzheimer's disease were solved using cryo-electron microscopy (Fitzpatrick *et al.*, 2017) shortly before I began this thesis project, verification and further investigation of the results remained as one of my goals for this project. By examining samples from patients diagnosed with either rpAD or spAD, I compared both the resulting electron micrographs and the 3D-reconstructions to the published data. This will provide evidence either for or against the conclusion from Falcon *et al.* (2018a) that the structure of tau PHFs and SFs is consistent across all Alzheimer's disease cases. In this thesis project I aim to answer the following: Are the structures of tau protein PHFs and SFs consistent across all cases of Alzheimer's disease?

The second aspect of this thesis project was the examination of mouse-derived 2N4R tau fibrils containing a disease causing P301L mutation. This mutation is found in some cases of FTDP-17 (Ghetti *et al.*, 2015), and as such these mice are used as a model

for this disease. Previous research completed by Eskandari-Sedighi *et al.* (2017) demonstrated that these mice display heterogeneity in the location of tau deposition in the brain which resulted in the creation of five pathology classes. Additionally, when the resulting brain homogenates are examined by EM, three different fibril morphologies are observed in variable proportions. As part of this thesis project I continued the examination of the three different fibril morphologies found in the five pathology classes. I examined primarily Class III tau filaments with electron microscopy, as this class was not previously examined in the publication (Eskandari-Sedighi *et al.*, 2017). Additionally, I completed 3D-reconstructions on fibrils from Class I-IV so that I could compare these structures both with each other and with other published tau structures. The questions that I aimed to answer in this portion of the thesis project was: Are the structures of the three observed tau fibril morphologies different from each other and other published tau structures? Are there meaningful differences in the proportion of the three tau fibril morphologies and does this contribute to disease?

Overall, the central hypothesis for this thesis project is that the tau protein can adopt numerous different conformations which contribute to the manifestation of different tauopathies and the differences seen between these tauopathies. This has been seen in the published tau fibril structures from AD (Falcon *et al.*, 2018a, Fitzpatrick *et al.*, 2017), CTE (Falcon *et al.*, 2019), PiD (Falcon *et al.*, 2018a), and CDB (Zhang *et al.*, 2020). In each of these diseases, the tau protein adopts fibril structures which are unique. I will provide additional evidence for this through EM examination and 3D-reconstruction of tau fibrils from AD and a mouse model of FTDP-17. Secondly, I hypothesize that the tau protein can adopt multiple conformations which all lead to the same disease but may explain the differences seen between individuals. I will do this through the examination of mouse-derived tau fibrils which model FTDP-17, a disease which displays high degrees of variation in disease manifestation and progression.

Chapter 2

Materials & Methods

2.1 Tau protein purification from mouse brain

Mouse brains were purified following the protocol from Sahara *et al.* (2013) by Ghazaleh Eskandari-Sedighi. Mouse brains were bisected down the midline, frozen on dry ice, and stored at -80°C until use. Tissues were homogenized in 10 volumes of tris-buffered saline (TBS: 50 mM Tris/HCl (pH 7.4), 274 mM NaCl, 5 mM KCl, 1% protease inhibitor mixture, 1% phosphatase inhibitor cocktail (Sigma), 1mM phenylmethylsulfonyl fluoride (PMSF)). The homogenates were centrifuged at 27,000xg for 20min at 4°C to obtain supernatant and pellet fractions. Pellets were homogenized in 5 volumes of high salt/sucrose buffer (0.8 M NaCl, 10% sucrose, 10 mM Tris/HCl, (pH 7.4), 1 mM EGTA, 1 mM PMSF)) and centrifuged at 27,000xg for 20min at 4°C. The supernatant was collected and incubated with 1% final concentration sarkosyl (Sigma) for one hour at 37°C followed by centrifugation at 150,000xg for one hour at 4°C to obtain salt and sarkosyl-extractable and sarkosyl-insoluble fractions. The sarkosyl-insoluble pellet was resuspended in TE buffer (10 mM Tris/HCl (pH 8.0), 1 mM EDTA) to volume equivalent to half that of the brains

used to produce brain homogenate. Following purification, a western blot with CP13 (detecting phosphorylated Ser202), CP27 (detecting total human tau protein), PHF1 (detecting phosphorylated S396 and S404), and ET3 (detecting 4R tau residues 273–288) antibodies was performed on the resuspended pellet to confirm the presence of the tau protein.

2.2 Tau protein purification from human brain

Human brain samples of the frontal cortex were purified by Chae Kim and Dr. Miroslava Kacirova. Slices were homogenized in 10 volumes of Tris-buffered saline (TBS: 50 mM Tris/HCl (pH 7.4), 274 mM NaCl, 5 mM KCl, 1% protease inhibitor mixture, 1% phosphatase inhibitor cocktail, 1mM phenylmethylsulfonyl fluoride (PMSF)). The homogenates were centrifuged at 27,000xg for 20min at 4°C to obtain supernatant and pellet fractions. Pellets were homogenized in 5 volumes of high salt/sucrose buffer (0.8 M NaCl, 10% sucrose, 10 mM Tris/HCl, (pH 7.4), 1 mM EGTA, 1 mM PMSF) and centrifuged at 27,000xg for 20min at 4°C. The supernatant was collected and incubated with 1% final concentration sarkosyl for one hour at 37°C followed by centrifugation at 150,000xg for one hour at 4°C to obtain salt and sarkosyl-extractable and sarkosyl-insoluble fractions. The sarykosyl-insoluble pellet was resuspended in water and protease inhibitor cocktail (0.5µg/mL aprotinin, 0.5µg/mL leupeptin, 0.05mM PMSF).

2.3 Negative stain electron microscopy

Aliquots of 1-3µL containing purified human or mouse derived tau fibrils were loaded on to freshly glow discharged 400 mesh carbon coated copper grids (Electron Microscopy Sciences) and absorbed for 1 minute. Grids were washed with 50µL each of 0.1M and 0.01M ammonium acetate and stained with 2x50µL of freshly filtered 2% uranyl

acetate. Once dry, grids were visualized with a Tecnai G20 transmission electron microscope (Thermo Fisher FEI) using an acceleration voltage of 200kV. Electron micrographs were recorded with an Eagle 4kx4k CCD camera (Thermo Fisher FEI).

2.4 3D fibril reconstruction

Micrographs which contained single, isolated tau fibrils with a visible crossover region were selected. Using EMAN's boxer program (Ludtke *et al.*, 1999), crossover regions were selected and segmented into overlapping boxes of 200 x 200 pixels spaced 1-5 pixels apart along the helix and centered using the unbend or align helix feature. Angles were assigned to each box, with the assumption that the selected region was 180° and that each box represented a different view of the same fibril. SPIDER operation Back Projection 3D (BP 3D) (Frank *et al.*, 1996) was used to generate a reconstruction using the box files and angular assignments. UCSF Chimera (Pettersen *et al.*, 2004) was used to visualize the reconstructions (Figure 2.1).

2.5 Cross-section rotation

The final 3D-reconstructions were used as a starting point. Using EMAN proc3D and align3D commands (Ludtke *et al.*, 1999), the reconstructions were normalized, aligned, and rotated 90°. The 3D map was converted into a stack of 2D particles, which were aligned to a reference image using EMAN until the resulting image did not change on subsequent iterations. The last 2D average image was centered using IMAGIC (van Heel *et al.*, 1996). The centered 2D cross-section was replicated 290x using the EMAN proc2D command. Using the IMAGIC rotate image command, the replicated cross sections were

rotated back 90° and the 2D projection was set to a 3D volume using the IMAGIC header command to yield the final fibril reconstruction (Figure 2.1).

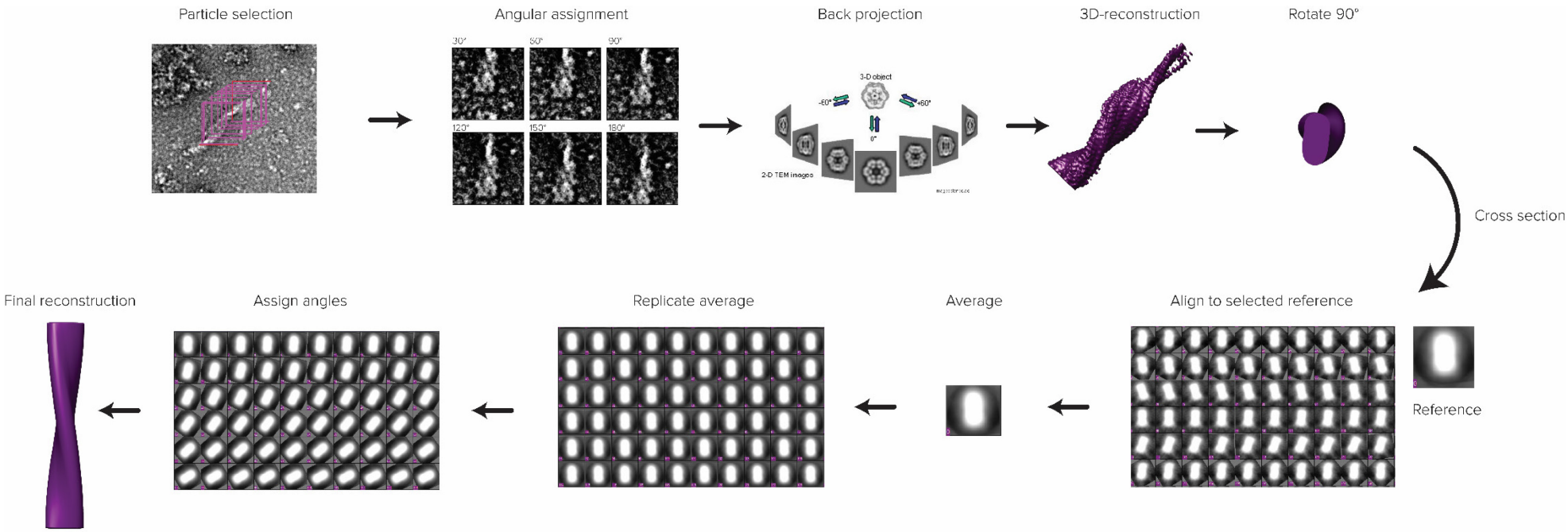

Figure 2.1. Overview of the 3D-reconstruction and cross-section rotation process. The first step in 3D-reconstruction is to place boxes along the crossover region of the fibril using boxer which then generates a series of images. These images represent the fibril at different angles. Angles are assigned to each image, and back projection generates a 3D-model of the original fibril. This model is rotated 90° and cross sectioned. A reference cross section is selected and used to align the cross sections. The resulting average is replicated, and angles are assigned to these images. The final reconstruction is generated by assembling the cross sections into a 3D-model.

Chapter 3

Structural Analysis of Mouse-derived Tau Protein Aggregates

3.1 Characterization of mouse-derived tau protein aggregates

One of the objectives of this thesis project was to characterize tau protein aggregates extracted from Tgtau^{P301L} mouse brains. These mice express a mutant version of the human form of tau, 2N4R, at low levels, making them an approximate model for FTDP-17. These mice have been previously characterized by Eskandari-Sedighi *et al.* (2017) using immunohistochemistry and Thioflavin S, Gallyas-Braak, and Bielschowsky staining procedures. They have been shown to slowly develop pre-tangles, granofibrillary tangles, and NFT-like structures in the CNS. However, the exact location of the tau deposition in these animals showed heterogeneity, which resulted in the creation of five pathological classes (I, II, III, IV, V) based on the location of tau deposition. (Figure 3.1) Preliminary electron microscopic characterization prior to the commencement of this project revealed that these animals present with three different tau fibril morphologies: straight, coiled, and twisted ribbon-like (Figure 3.2). The proportions of these fibril

morphologies varied between pathology classes. The continued structural characterization of the three filament morphologies using electron microscopy and 3D-reconstruction is of interest as it will allow for comparison not only between the three morphologies but also with published tau structures which will contribute to the tau strain hypothesis (Gerson *et al.*, 2016, Sanders *et al.*, 2014).

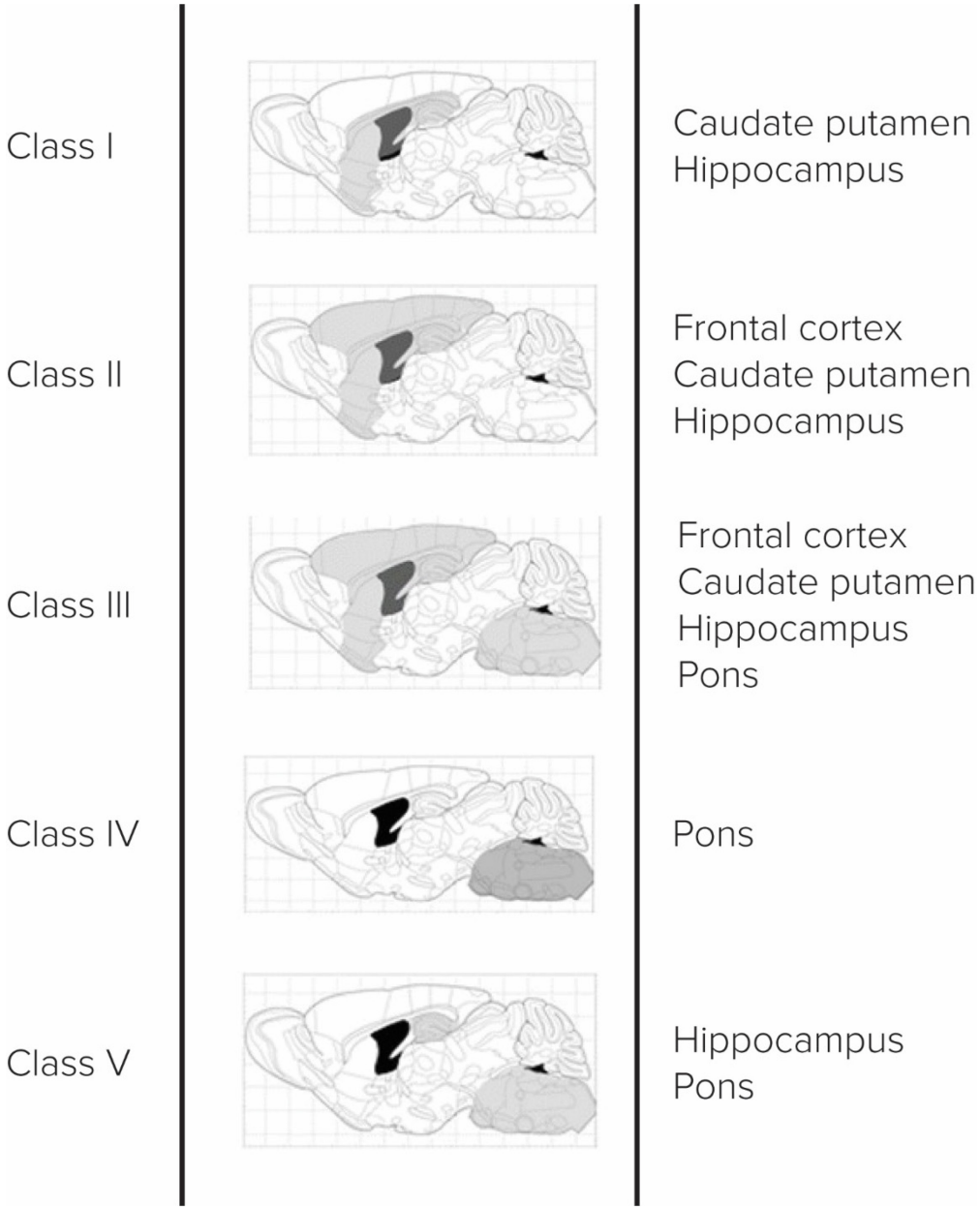

Figure 3.1. The five mouse pathology classes. Mouse brain sagittal cross sections in middle column display the primary locations of tau pathology (grey) for each of the five classes. The primary locations of tau pathology are also listed in the right-hand column. This figure was adapted and reproduced with permission under the Creative Commons Attribution 4.0 International license (http://creativecommons.org/licenses/by/4.0/) from Eskandari-Sedighi *et al.* (2017).

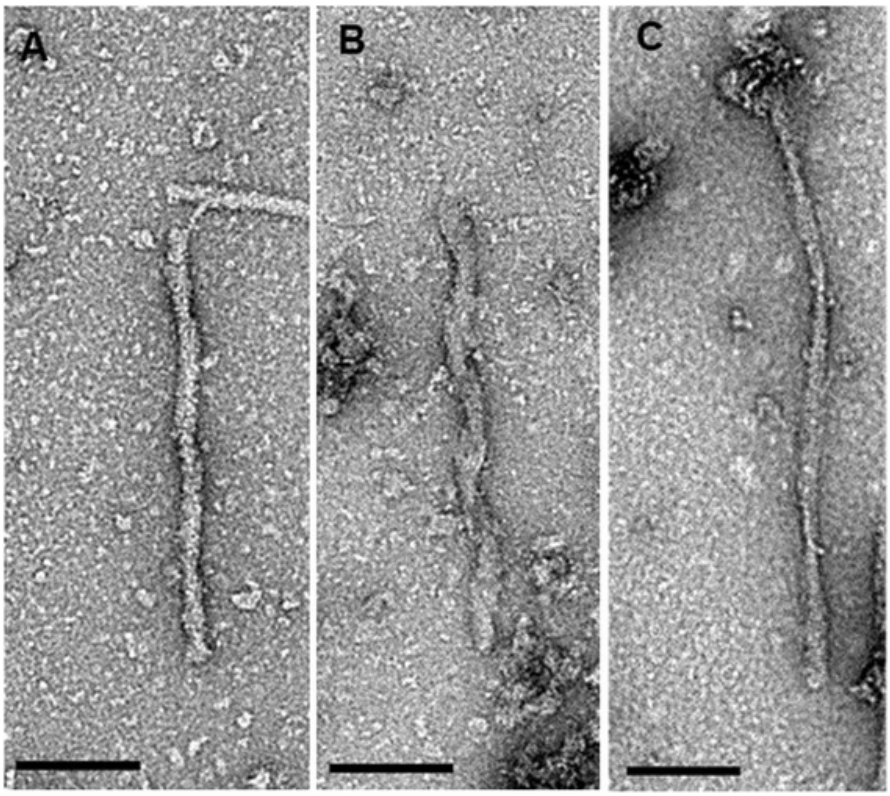

Figure 3.2. Electron micrographs of mouse-derived tau fibrils. Three different fibril morphologies are shown: straight (a), coiled (b), and twisted ribbon-like (c). Scale bars are 100nm. This figure was reproduced with permission under the Creative Commons Attribution 4.0 International license (http://creativecommons.org/licenses/by/4.0/) from Eskandari-Sedighi *et al.* (2017).

3.1.1 Electron microscopic characterization of mouse-derived tau protein aggregates

Purified tau fibril samples from pathology classes I, II, III, and IV were observed with EM as described in section 2.3. The focus was primarily on class III samples, as the other classes have been previously characterized in the publication by Eskandari-Sedighi *et al.* (2017). In total, seven class III samples were visualized, along with one class I, and two class IV. A 'typical' micrograph for the samples in shown in Figure 3.3a. Class III samples are composed almost exclusively of straight fibrils (Figure 3.3b); 82.3% in fibril counts. The remaining fibrils are twisted ribbons, 3.1%, or fibrils that were obscured or do not fit into the classification system (Table 3.1). Data for class I, II, and IV from Eskandari-Sedighi *et al.* (2017) is displayed in Table 3.2.

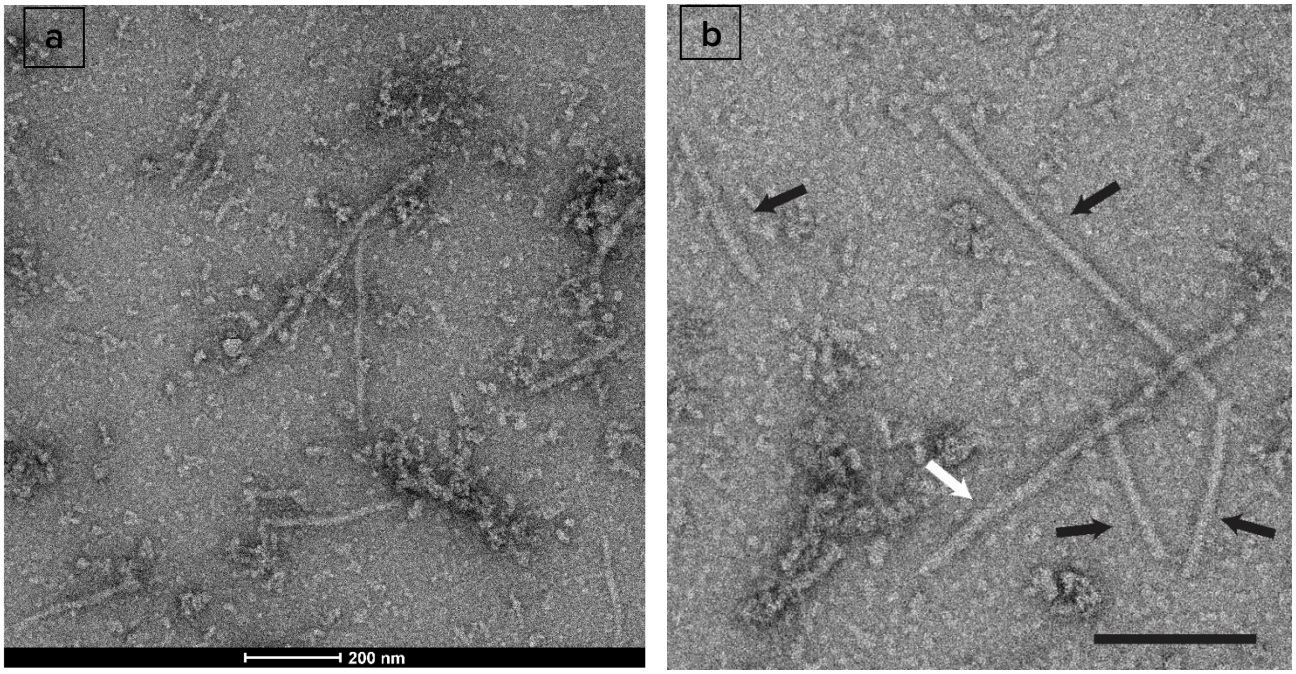

Figure 3.3. Electron micrographs of tau fibrils from class III samples. Negative stain electron microscopy was performed on pathology class III insoluble tau fractions. **a.** A representative micrograph of a typical class III sample. **b.** Electron micrograph displaying straight fibrils (black arrows) and twisted ribbon-like fibrils (white arrow). Scale bars are 200nm.

Table 3.1. Distribution of tau fibril morphologies in pathology class III. N refers to the number of distinct samples for which fibril counts were completed.

N	Straight Fibril	Coiled Fibril	Twisted Ribbon-like Fibril	Other
7	127	0	4	15
	80%	0%	3%	17%

Table 3.2. Distribution of tau fibril morphologies according to pathology class. N refers to the number of distinct samples for which fibril counts were completed. Mouse line refers to the genetic background of the P301L mice used. This table was adapted and reproduced with permission under the Creative Commons Attribution 4.0 International license (http://creativecommons.org/licenses/by/4.0/) from Eskandari-Sedighi *et al.* (2017).

Mouse lines	Pathology Class I				Pathology Class II				Pathology Class IV			
		Fibril Types				Fibril Types				Fibril Types		
	N	Straight Fibril	Coiled Fibril	Twisted Ribbon-like Fibril	N	Straight Fibril	Coiled Fibril	Twisted Ribbon-like Fibril	N	Straight Fibril	Coiled Fibril	Twisted Ribbon-like Fibril
C57BL/6	2	39	35	1	2	189	0	0	3	6	0	0
		52%	47%	1%		100%	0%	0%		100%	0%	0%
129SvEv	1	22	0	1	1	55	0	0	3	23	0	0
		96%	0%	4%		100%	0%	0%		100%	0%	0%
FVB/NJ	2	21	0	0	3	121	1	0	3	14	0	0
		100%	0%	0%		99%	1%	0%		100%	0%	0%

3.1.2 3D-reconstruction and measurements of mouse-derived tau protein aggregates

Collected electron micrographs were processed as described in sections 2.4 and 2.5 to generate 3D models of the tau fibrils. At least one fibril from each class was reconstructed. The twisted ribbon-like fibrils were reconstructed easily, while the straight and coiled fibrils posed additional challenges. The straight fibrils lack an easily identifiable crossover region and therefore require a system of trial-and-error to determine the correct location to select. The coiled fibrils often curve so much that the boxer software (Ludtke *et al.*, 1999) cannot properly select the fibril. To counter this, they must first be 'straightened' by rotating the image so that the fibril is vertical in the desired area for reconstruction.

Once reconstructed, the fibrils from each pathology class and morphology were compared to one another. The structure of fibrils of the same morphology remained consistent despite the pathology class, i.e. twisted ribbon-like fibrils from class III are the same as twisted ribbon-like fibrils from class I. This was found to be the case for all fibril morphologies (Figure 3.4).

Measurements of width and helical pitch were completed for fibrils of each morphology using the 'ruler' tool in Adobe Photoshop. The widths of the fibrils, while seemingly similar to each other, displayed significant differences. The average width of straight fibrils was 21.7nm for class I, 19.7nm for class II, 16.5nm for class III, and 21.9nm for class IV (Table 3.3). Pairwise t-tests resulted in $p < 0.01$ for all comparisons, except for class I and IV straight fibrils which resulted in $p > 0.05$. An ANOVA analysis of straight fibrils from all classes resulted in $p < 0.01$. The average width of coiled fibrils was 26.3nm for class I and 25.9nm for class II (Table 3.3). A pairwise t-test nor an ANOVA was possible for this fibril morphology as only one coiled fibril was measured from class II. The average width of twisted ribbon-like fibrils was 23.2nm for class I and 20.5nm for class III (Table 3.3) with a pairwise t-test resulting in $p > 0.05$; an ANOVA analysis was not possible for

twisted ribbon-like fibrils. The helical pitch was found to differ for coiled and twisted ribbon-like fibrils. Coiled fibrils have a larger average helical pitch, 136.9nm for class I and 141.7nm for class II, compared to twisted ribbon-like fibrils, 82.1nm for class I and 75.9nm for class III (Table 3.3). A pairwise t-test was not possible for coiled fibrils as only one fibril was measured from class II, but a pairwise t-test for twisted ribbon-like fibrils result in $p > 0.05$; an ANOVA analysis was not possible for helicity measurements.

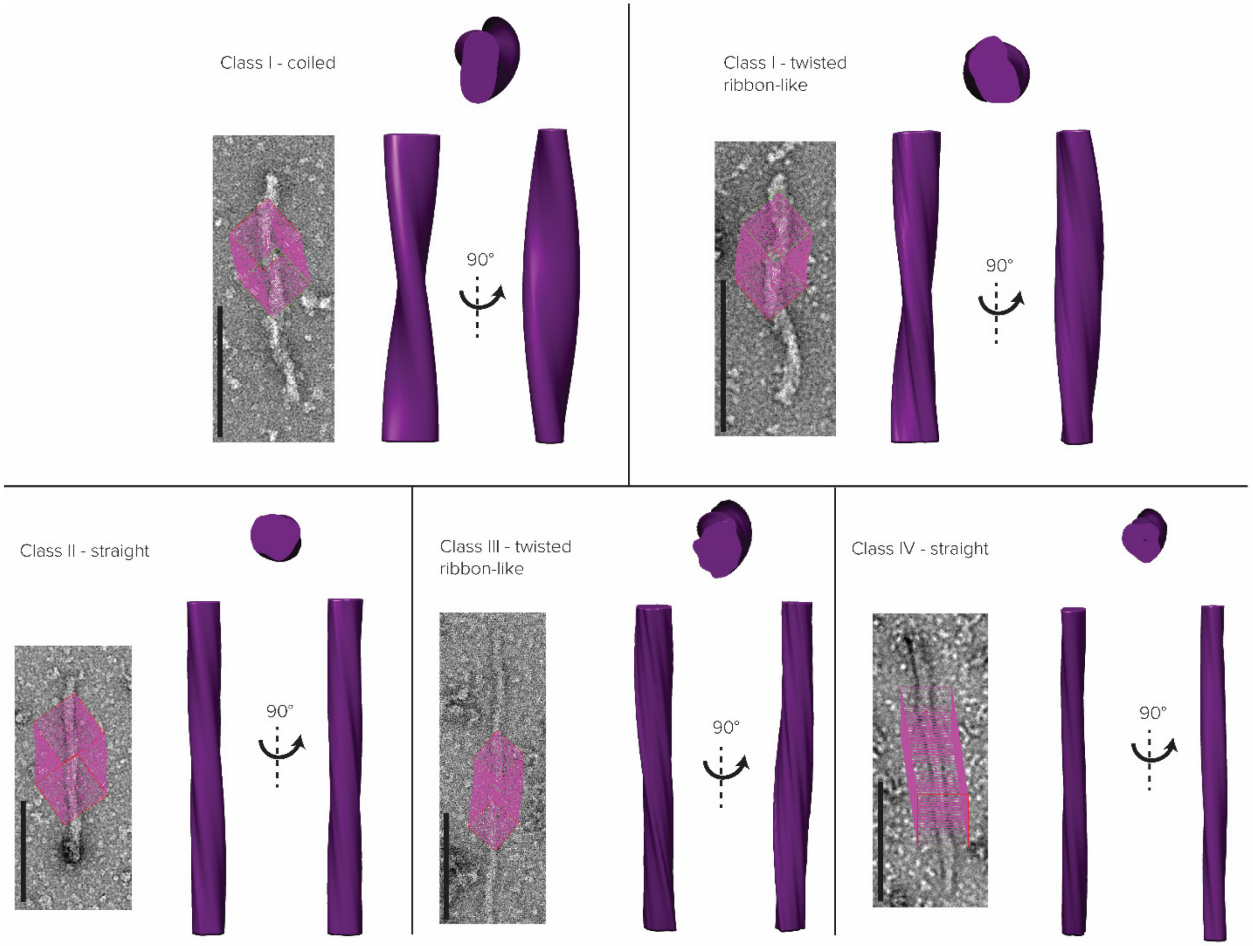

Figure 3.4. 3D-reconstructions of fibrils from mouse pathology classes I-IV. Top left panel corresponds to a coiled fibril from mouse pathology class I and top right panel corresponds to a twisted ribbon-like panel from mouse pathology class I. Bottom left panel corresponds to a straight fibril from mouse pathology class II. Bottom middle panel corresponds to a twisted ribbon-like fibril from mouse pathology class III. Bottom right panel corresponds to a straight fibril from mouse pathology class IV. All 3D-reconstructions were width matched with the measurements from electron micrographs. Two side views and a top view is shown for each. Scale bars are 200nm.

Table 3.3 Width and helical pitch measurements of tau fibrils from pathology classes I-IV. N refers to the number of distinct fibrils for which measurements of width and helical pitch were made.

	N	Class I	N	Class II	N	Class III	N	Class IV
Straight Fibril Width (nm)	59	21.7 +/- 2.7	143	19.7 +/- 2.4	70	16.5 +/- 5.1	28	21.9 +/- 2.7
Coiled Fibril Width (nm)	24	26.3 +/- 4.3	1	25.9		--		--
Coiled Fibril Helical Pitch (nm)	17	136.9 +/- 22.4	1	141.7		--		--
Twisted Ribbon-like Fibril Width (nm)	5	23.2 +/- 3.7		--	6	20.5 +/- 7.9		--
Twisted Ribbon-like Fibril Helical Pitch (nm)	4	82.1 +/- 9.8		--	4	75.9 +/- 1.6		--

Chapter 4

Structural Analysis of Human-derived Tau Protein Aggregates

4.1 Characterization of human-derived tau protein aggregates

The second objective of this thesis project was to examine tau fibrils which were purified from AD patient brains. We obtained samples from sporadic AD (sAD) cases, including rpAD and spAD. The rpAD samples used for analysis were collected from donors of 57, 64, and 66 years in age at the time of death and the spAD samples were collected from a donor of 90 and 67 years in age. The initial characterization of these samples was completed by Chae Kim and Dr. Miroslava Kacirova in Dr. Jiri Safar's laboratory at Case Western Reserve University. They performed western blots, silver staining, and conformation-dependent immunoassay (CDI) on the samples and found that preliminary CDI data suggested differences in the structural organization of rpAD and spAD tau aggregates and in the organization of fAD tau aggregates (Figure 4.1). Briefly, CDI is a technique which allows for quantification of a protein's resistance or susceptibility to denaturation. Through the use of primary antibodies specific to tau in its native and

denatured form and secondary antibodies which allow for signal detection, it is possible to measure the amount of tau in the native or denatured conformation, before and after exposure to a strong denaturant. It is the difference in the denatured/native (D/N) value that can suggest differences in structural organization (Daude *et al.*, 2020, Safar *et al.*, 1998). Through additional characterization with electron microscopy, I will expand on the initial CDI results for rpAD and spAD; fAD will not be addressed in this thesis as no fAD samples were received. Based on the similarities and/or differences seen between samples from rpAD and spAD, I can determine if the structure of the tau protein plays a role in how AD develops and progresses.

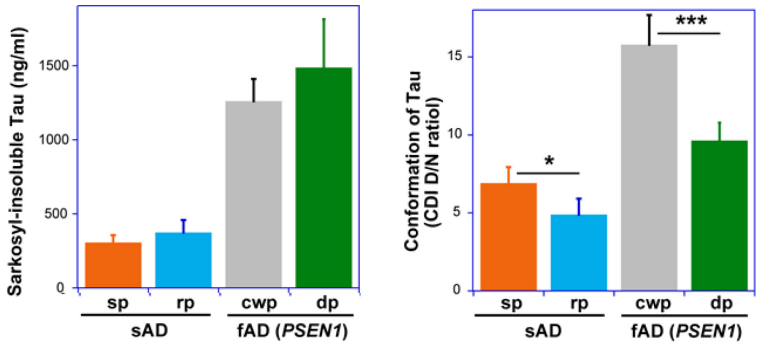

Figure 4.1. Levels and conformational characteristics of sarkosyl-insoluble tau in sAD and fAD. CDI was carried out on sarkosyl-insoluble tau from spAD (orange), rpAD (blue), fAD with cotton wool plaques (grey), and fAD with dense plaques (green). The levels of sarkosyl-insoluble tau were quantified (right panel). fAD has approximately 3-fold higher levels of sarkosyl-insoluble tau than sAD. CDI data (left panel) suggests that the conformation of tau in spAD and rpAD was statistically significant and that the conformation of tau in fAD cotton wool plaques and dense plaques was also significant, although the difference was more significant in fAD. This figure was provided for use by Dr. Jiri Safar.

4.1.1 Electron microscopic analysis of human-derived tau protein aggregates

Purified tau fibril samples from rpAD and spAD were observed with EM as described in section 2.3. In total, four cases of rpAD and three cases of spAD were analyzed with EM. Overall, the quality of the samples was inconsistent, with some samples having many fibrils and others having next to none. Only two rpAD and one spAD sample yielded fibrils on which further analysis could be completed. In these samples both PHFs and SFs were observed (Figure 4.1), with PHFs being the more prominent species. PHFs display a noticeable 'fuzzy' crossover region, while SFs do not. The proportion of PHFs to SFs was approximately equivalent for rpAD at spAD cases; 64.4% and 77.1% for PHFs in rpAD and spAD, respectively; and 35.6% and 22.9% for SFs in rpAD and spAD, respectively (Table 4.1).

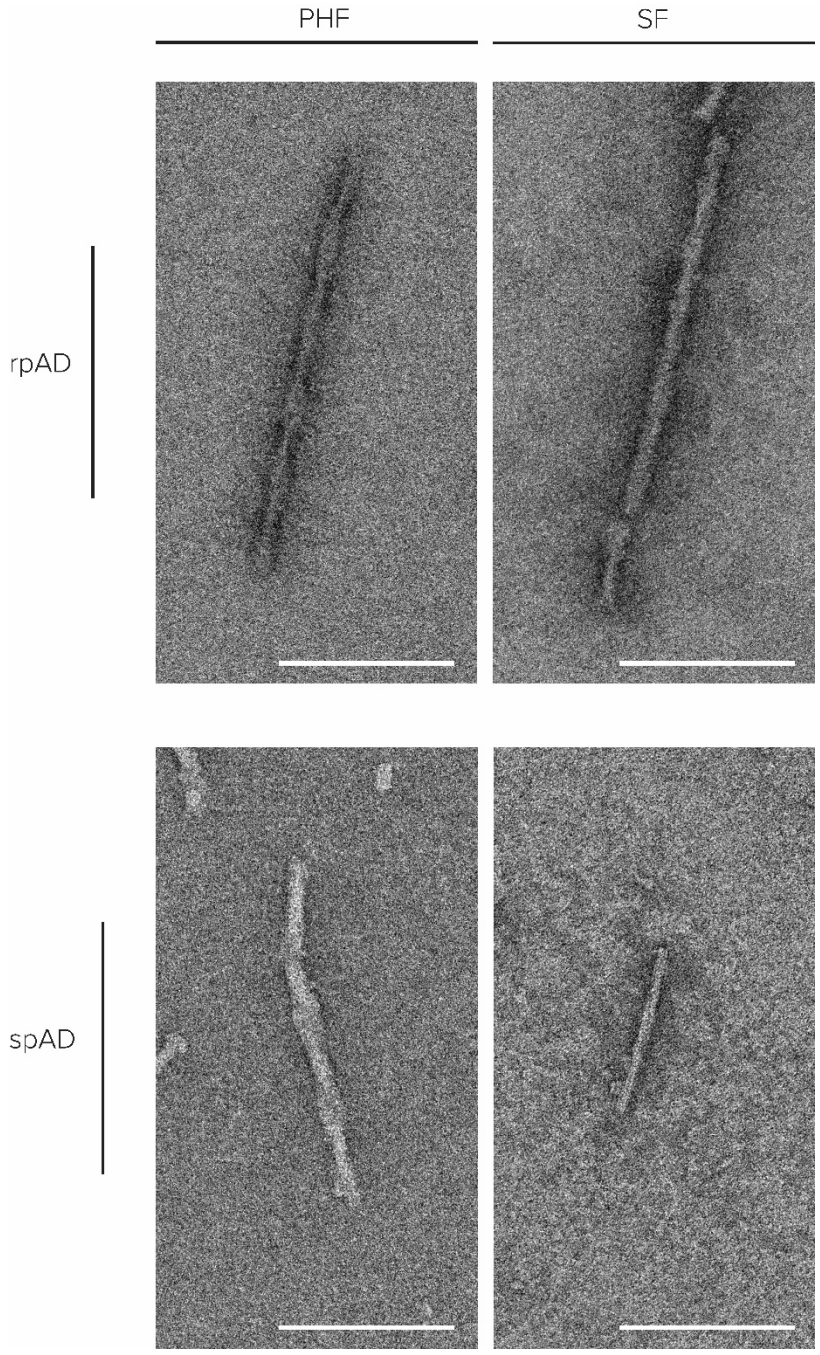

Figure 4.2. Electron micrographs of PHFs and SFs fin rpAD and spAD cases. Negative stain electron microscopy was performed on samples from rpAD and spAD. Both PHFs and SFs were present in both types of AD. PHFs can be distinguished by ‘fuzzy; regions interspaced by sharp, narrow regions. SFs do not contain this ‘fuzzy’ region. Scale bars are 200nm.

Table 4.1. Fibril counts of PHF and SF in rpAD and spAD cases. N refers to the number of distinct samples for which fibrils were counted.

	N	PHFs	SFs
rpAD	3	58 64.4%	32 35.6%
spAD	2	47 77.1%	12 22.9%

4.1.2 3D-reconstruction of human-derived tau protein aggregates

Collected electron micrographs were processed as described in sections 2.4 and 2.5 to generate 3D models of the tau fibrils. Only PHFs from both rpAD and spAD were reconstructed, as the micrographs collected of SFs were not of adequate quality for 3D-reconstruction; the fibrils were either too short or obstructed by other fibrils. Additionally, SFs have the added challenge of lacking a visible crossover region. The reconstructed PHFs from rpAD and spAD appear similar to each other. Both reconstructions display a clear, narrow crossover region, corresponding to the narrow region seen in the micrographs, and a wider region, corresponding to the 'fuzzy' region seen in the micrographs (Figure 4.3).

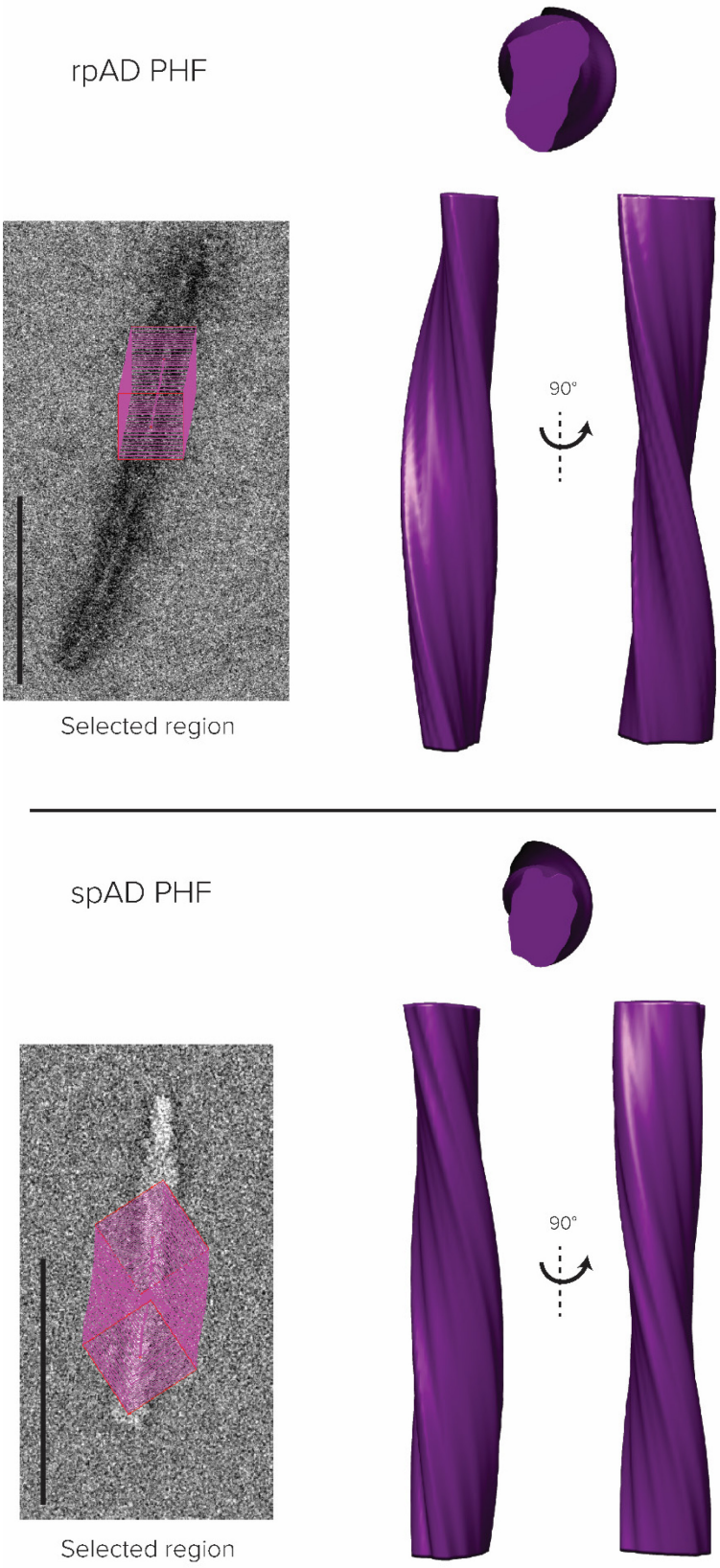

Figure 4.3. 3D-reconstruction of PHFs from rpAD and spAD. Top panel corresponds to the reconstruction of a rpAD PHF and bottom panel corresponds to the reconstruction of a spAD PHF. Pink boxes on electron micrographs highlight the region which was selected for reconstruction. The generated 3D-reconstructions were width-matched with measurements from the electron micrographs. Two side views and a top view is displayed for both the rpAD PHF and the spAD PHF. Visual comparison between the two 3D-reconstructions show strong similarity between each other. Scale bars are 200nm.

Measurements of width and helical pitch were completed for PHFs and SFs from rpAD and spAD using the 'ruler' tool in Adobe Photoshop. PHFs were found to have variable average widths, ranging from 23.2m and 26.1nm at the widest point in rpAD and spAD, respectively, to 8.8nm and 10.0nm at the narrowest point in rpAD and spAD, respectively (Table 4.2). Paired t-tests for the width of PHFs from rpAD and spAD at the widest point resulted in $p < 0.01$ and a paired t-test for the width of PHFs from rpAD and spAD at the narrowest point resulted in $p < 0.01$. SFs did not display variability in their width. The average width of SFs in rpAD was 12.1nm and 14.9nm in spAD and a paired t-test resulted in $p < 0.05$. The average helical pitch of PHFs in rpAD and spAD was 89.2nm and 92.9nm (Table 4.2), respectively, and a paired t-test resulted in $p > 0.05$. The helical pitch of SFs was not measured as they do not have an obvious crossover region.

Table 4.2. Width and helical pitch measurements of PHFs and SFs from rpAD and spAD cases. N refers to the number of distinct measurements made for width and helical pitch.

	N	rpAD	N	spAD
PHF Narrowest Region Width (nm)	39	8.8 +/- 1.6	39	10.0 +/- 1.8
PHF Widest Region Width (nm)	39	23.2 +/- 3.8	39	26.1 +/- 3.6
PHF Helical Pitch (nm)	36	89.2 +/- 10.1	45	92.9 +/- 17.6
SF Width (nm)	19	12.1 +/- 2.2	8	14.9 +/- 3.3

Chapter 5

Discussion

5.1 Structural comparison of mouse-derived tau filaments and relevance to disease

The mouse-derived tau filaments have three distinct morphological differences, which resulted in the creation three categories: straight fibrils, coiled fibrils, and twisted ribbon-like fibrils (Eskandari-Sedighi *et al.*, 2017). These morphological differences are readily visible by eye and reinforced by quantitative measurements of width and helical pitch. Straight, coiled, and twisted ribbon-like can be considered three unique structures that the tau protein can adopt. This result is consistent with past studies of tau fibrils from FTDP-17. EM studies of fibrils extracted from individuals with FTDP-17 with a P301L tau mutation revealed filaments of irregular twisted ribbons and straight filaments with a stranded rope appearance (Spillantini *et al.*, 1998) (Figure 5.1). Another study which observed tau fibrils from P301L tau transgenic mice found fibril results consistent with those found in humans (Götz *et al.*, 2001). The twisted ribbon and stranded rope morphologies observed by these two studies remain consistent with fibrils we observed and classified as coiled and twisted ribbon-like, respectively, however the straight fibrils

we found differ from the two previously described morphologies as there is a lack of any observable crossover. In both studies (Götz *et al.*, 2001, Spillantini *et al.*, 1998), researchers completed measurement of width and helicity. Twisted ribbon filaments from human origin were found to have a width of about 15nm and a helical pitch of greater than 130nm (Spillantini *et al.*, 1998). The width of the straight, stranded rope fibrils was about 12nm (Spillantini *et al.*, 1998). Twisted ribbon filaments of transgenic mouse origin also had a width of about 15nm (Götz *et al.*, 2001). These measurements are not identical to what we found when completing width and helicity measurements on the fibrils from our Tgtau^{P301L} mice (Figure 3.3). Straight fibrils from pathology class III have a width which is the most similar to those previously found, having a width of about 16nm. The remainder of the width measurements completed were larger than the previous measurements, with the widest fibril measurement of about 25nm being from coiled fibrils. This difference can likely be accounted for by the selected area for measurements. In the fibril measurements completed here, the largest section of coiled and twisted ribbon-like fibrils was selected. Measurement of the narrowest portion of the fibril would result in a smaller width measurement. The researchers who completed measurements on FTDP-17 filaments previously (Götz *et al.*, 2001, Spillantini *et al.*, 1998) do not specify which region, widest or narrowest, is measured. The measurements of helical pitch are most similar to the previous results in the coiled fibrils, which was measured to be greater than 130nm. Twisted ribbon-like fibrils were found to have a smaller pitch of about 80nm, however the previous researchers did not complete measurements for the fibrils which appear most similar to twisted ribbon-like fibrils in our classification system. Overall, the measurements completed on the different fibril morphologies are fairly consistent with previously published results. Currently, these published electron micrographs and measurements are the only insight to the structure of the tau protein in FTDP-17; there is not a high-resolution structure available. The 3D-reconstructions I have generated based on the electron micrographs and confirmed fibril measurements provide the framework for

further high-resolution models as the models I have generated represent the architecture of three tau fibril morphologies seen in FTPD-17 cases.

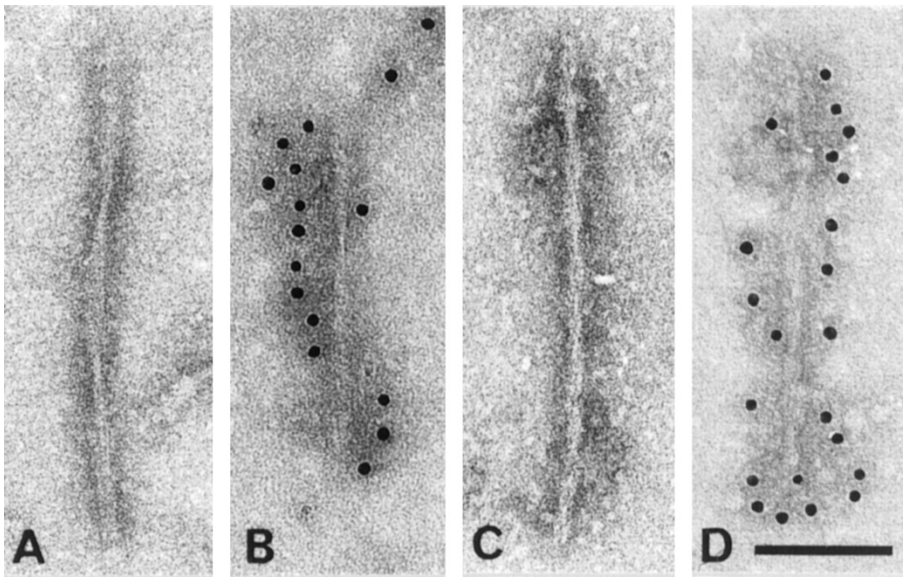

Figure 5.1. Electron micrographs of tau filaments from FTDP-17 with a P301L mutation. Panels A and B show twisted ribbon fibrils and panels C and D show stranded rope fibrils. Panels B and D show immuno-gold labelling of the tau filaments with a phosphorylation dependent anti-tau antibody AT8. Scale bar is 100nm. This figure was reproduced from The American Journal of Pathology, Volume 153, Issue 5, M.G. Spillantini, R.A. Crowther, W. Kamphorst, P. Heutink, J.C. van Swieten, Tau Pathology in Two Dutch Families with Mutations in the Microtubule-Binding Region of Tau, Pages 1359-1363, Copyright 1998 with permission from Esevier.

The architecture of the three mouse-derived tau fibril morphologies remained consistent across all pathological classes, however the proportion of the morphologies varied. Straight fibrils were the most common in all classes observed and the amounts of coiled and twisted ribbon-like fibrils varied. Only classes I and II contained coiled fibrils and classes I and III contained twisted ribbon like-fibrils. Overall, class I displayed the most variability in the observed fibril morphologies while classes II-IV were almost exclusively composed of straight fibrils. The observed difference in the proportion of tau fibril types may be related to the difference in tau pathology distribution. Certain areas of the brain may tend to develop one fibril morphology over another. This is difficult to prove as it would require the isolation and examination of individual mouse brain regions; it is only possible to speculate about which brain areas tend to develop each fibril morphology. It is also be possible that the different fibril morphologies represent the progression of disease. Straight fibrils, being the most common, may be the first morphology to develop. The coiled and twisted ribbon-like fibrils then appear as the disease progresses. The opposite could also be true, with the less common coiled and twisted ribbon-like types undergoing an unknown conformational change to become straight fibrils as disease progresses. Presently, the data collected does not provide significant evidence for either possibility, however it does not completely rule them out. To confirm one of these possibilities, time course experiments would be necessary. Through examination of the tau fibril species present at different time points in disease we could determine if the fibrils morphology correlates with disease progression.

A future experiment which would provide supporting data for the similarities and differences between the three tau fibril morphologies is immuno-EM. This technique involves the use of antibody labelled gold particles which are expected to bind to your protein of interest, in this case the tau protein. The sample and antibody-linked gold particles bind and are absorbed on to a grid for EM visualization. This experiment would confirm that the fibrils we observe are the tau protein if we see tau fibrils ‘decorated’ with

gold particles (Figure 5.1). Using antibodies that bind different regions of the tau protein, i.e. R1, R2, R3, R4, we could determine which regions of the tau protein are in the fibril core and which are in the fuzzy coat (Falcon *et al.*, 2018b, Götz *et al.*, 2001). Currently, this technique is not able to differentiate different fibril conformations, i.e. AD fibrils vs PiD fibrils, from one another as there are no available antibodies that bind different tau isoforms differently. However, if antibodies capable of this were available, this technique would provide strong evidence for the presence of different tau fibril conformations. The immuno-EM can be compared to the results from AD tau fibrils, or other tauopathies, to provide a more in-depth analysis of the similarities and differences between different tau fibril structures.

In future experiments it would be also useful to collect additional micrographs using cryo-EM. Cryo-EM and the subsequent image processing can generate high resolution structural models of your protein of interest. This would require numerous quality control and optimization steps to prepare the mouse-derived tau samples and the collection of thousands of electron micrographs. With this data we could generate an atomic resolution model of the three tau fibrils found in the mouse-derived tau samples. An atomic resolution model would allow us to definitively determine if the three tau morphologies represent novel conformations of the tau protein in mice.

Finally, to confirm the relevance of the mouse-derived tau fibrils, EM characterization of human-derived FTDP-17 samples, specifically with the tau P301L mutation, would be required. Human derived FTDP-17 fibrils have been previously characterized by negative stain EM (Spillantini *et al.*, 1998), however this was done many years ago when cryo-EM was not well developed. Following the previously established protocol (Spillantini *et al.*, 1998), tau can be purified from the human samples. Preparation of the sample for cryo-EM will require optimization, as there is not currently published literature. Once analysis is complete, the generated structural models of human FTDP-17

tau with a P301L mutation can be compared to those which I have generated from mouse-derived tau samples and to those which have been published for tau in AD (Falcon *et al.*, 2018b, Fitzpatrick *et al.*, 2017), PiD (Falcon *et al.*, 2018a), CTE (Falcon *et al.*, 2019), and CBD (Zhang *et al.*, 2020). By comparing the tau fibril structure from FTDP-17 with the tau structure from these four diseases, we would be able to determine if the structure of tau fibrils in FTDP-17 represent novel conformations.

5.2 Structural comparison of human-derived tau filaments and relevance to disease

As described in Chapter 4, there were no visible differences between the PHFs in rpAD or spAD which is consistent with results published by Falcon *et al.* (2018b) where they visualized purified tau fibrils from both sporadic and inherited AD using cyro-EM. They found that the structure of PHFs and SFs did not vary between individual cases of AD. The reconstructions of PHFs which I generated provide additional evidence for this finding. In this project, we used different methods to purify, visualize, and reconstruct fibrils from human sAD samples. Our purification protocol differs in centrifugation speeds and lengths, and protease inhibitor use. To visualize the purified tau fibrils, I used negative stain EM, while the Falcon group used cryo-EM (Falcon *et al.*, 2018b, Fitzpatrick *et al.*, 2017). This means that our results are lower resolution. It is only possible to see the architecture of the tau fibrils in the reconstruction. However, this is adequate for the purpose of this thesis as it allows for the comparison of the overall structure of the tau PHF. An overlay of the AD core generated by Fitzpatrick *et al.* (2017) (PDB 5o3l) with the top view from my rpAD PHF reconstructions shows that the tau fibril core can fit into the 3D-model I generated and a side-by-side comparison shows similarities in the fibril architecture (Figure 5.2).

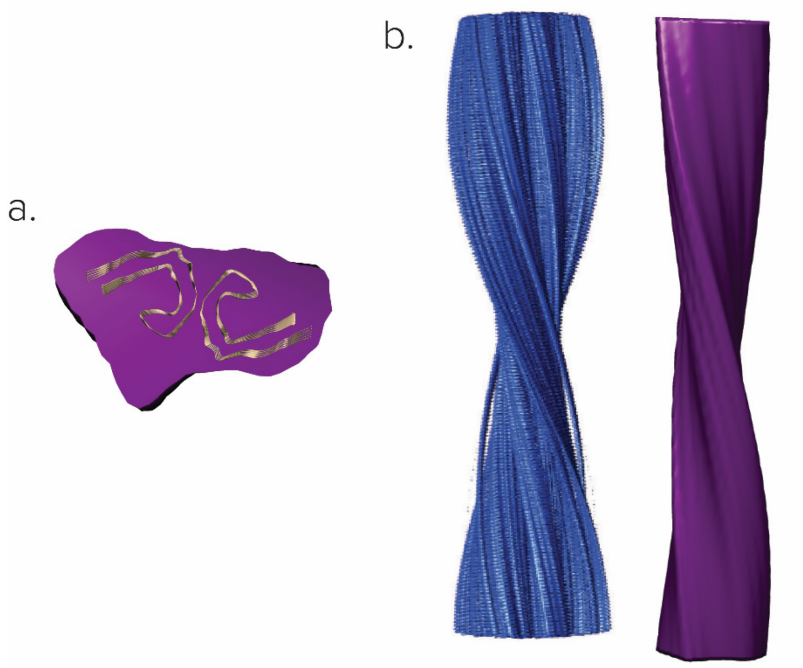

Figure 5.2. Top view and side-by-side comparison of tau PHF 3D-reconstructions with published structure. a. The tau core structure of tau PHF (brown) (PDB 5O3L) was overlaid on the top-view of the 3D-reconstruction from a rpAD PHF (purple). The two protofilaments can be fit into the fibril structure. **b.** Side-by-side comparison of published PHF fibril (blue) (This figure was adapted and reproduced with permission from Springer Nature Customer Service Centre GmbH: Springer Nature, Nature, Cryo-EM structures of tau filaments from Alzheimer's disease, Anthony W. P. Fitzpatrick *et al.* 2017) with generated 3D-reconstruction (purple).

Fitzpatrick *et al.* (2017) also completed measurements of width and helicity on the PHFs and SFs they observed. They found that PHF had a width of 150Å, or 15nm, at the widest area and 70Å, 7nm, at the narrowest. These measurements are approximately consistent with the measurements completed for the PHFs I observed. They were found to have a width of about 25nm at the widest area and 10nm at the narrowest. Helicity measurements were also completed for PHFs. Fitzpatrick *et al.* (2017) found that the spacing between crossovers ranged from 650-800Å, or 65-80nm. Our helical pitch measurement of about 90nm is similar to the published findings. Measurements for SFs are also approximately equivalent, with Fitzpatrick *et al.* (2017) measuring the width to be 100Å, or 10nm, and our recorded width for SFs being about 15nm. They also completed measurements of helical pitch for SFs, recording the distance between crossovers as between 700 and 900Å. We did not complete measurements of helical pitch for SFs as our micrographs were not of sufficient quality to identify the crossover region of the fibril. Overall, the measurements which I completed for width and helicity on tau PHFs and SFs provide another level of confirmation for our data. While the measurements are not identical to that of Fitzpatrick *et al.* (2017), they are likely within an acceptable range, as in Götz *et al.* (2001) the researchers recorded a width of about 20nm for AD PHFs and SFs. These differences can likely be accounted for by subtle differences in fibril appearance due to stain selection, or lack of in the case of Fitzpatrick *et al.* (2017), the use of different software to complete fibril measurements, and simple human error, as these measurements must be done by hand and a certain amount of variability between those completing the measurements is expected. Based on the comparison of quantitative measurements, fibril appearance, and 3D-reconstructions with published data I can conclude that we observed PHFs and SFs from AD patients which are consistent with published data.

In the future, it would be beneficial to complete 3D-reconstructions of SFs from AD samples. This would allow for a complete comparison of both PHF and SF tau fibril

structures to each other and to the published structures. Additionally, samples from fAD should be characterized. At this point, it is only possible to say that the structure of PHF from sAD is consistent between the 3D-reconstructions I have generated and the published models. Characterization of fAD samples would provide a more complete analysis of the tau fibril structures in AD. In their second paper, Falcon *et al.* (2018b) examined 15 sAD cases and 2 fAD cases. By characterizing additional fAD cases, I could provide stronger support for the arguments that the structure of PHFs and SFs remains consistent across all cases of AD, regardless of disease type. Overall, the reconstructions I have generated provide strong support for the published PHF structure, but more work is needed to confirm the SF structure.

Additional confirmation experiments, immuno-EM and cryo-EM, which were described for the mouse FTDP-17 samples, would also be applicable to the human AD samples. Immuno-EM would allow for identification of specific regions of the tau protein in PHFs and SFs. If the selected gold-conjugated antibodies bind to the tau fibrils, we know that region is present and accessible by the antibodies. This would provide confirmation that we are visualizing and reconstruction tau fibrils and that the predicted regions are present in the fuzzy coat and core of the fibril (Falcon *et al.*, 2018b, Fitzpatrick *et al.*, 2017). Cryo-EM characterization of the human AD samples would allow us to collect higher resolution information. This would therefore increase the resolution of the reconstructions to atomic level. The higher resolution reconstructions could be more directly compared to the published models (Falcon *et al.*, 2018b, Fitzpatrick *et al.*, 2017) and would provide stronger confirmation for the structure of PHFs and SFs.

The knowledge that PHFs and SFs have a consistent structure is advantageous to the development of treatments for AD. If we know that the structure the tau protein adopts does not change in different forms of AD, we can develop a way to target this specific structure. Already researchers are exploring therapies, such as β-breakers and anti-

aggregation agents, which target tau aggregation (Buee, 2019). Knowledge of the structure of PHFs and SFs in AD will allow researchers to design better drugs which target tau aggregation, potentially through rational drug design. By preventing the assembly of tau into disease driving PHFs and SFs, it may be possible to slow the progression or completely prevent AD.

5.3 Comparison of mouse and human-derived tau filaments

The structure of tau fibrils from the mouse and human sources differ significantly from each other. The fibrils in the FTDP-17 mouse model adopt different conformations from the fibrils in human AD. This is confirmed by width and helicity measurements from each disease. Straight fibrils from mouse pathology class III are the most similar to human SFs, with widths of 16.52nm (mouse straight fibrils) and 12.24nm (rpAD) and 15.89nm (spAD). However, the difference is enough to potentially allow for variability in the fibril structure. Human AD PHFs are most similar in width to coiled and twisted ribbon-like fibrils from mouse FTDP-17 samples, with widths of 24.34nm (rpAD), 26.42nm (spAD), 26.31nm (class I, coiled), and 23.16nm (class I, twisted ribbon-like). However, measurements of helical pitch are different for these fibrils, with PHFs having helical pitches of 91.52nm (rpAD) and 90.73nm (spAD), coiled fibrils having a helical pitch of 136.96nm (class I), and twisted ribbon-like fibrils having a helical pitch of 82.05nm (class I). The difference in helical pitch indicates that while the core structure may be similar, the stacking differs, allowing differences in helicity. The finding that the structure of tau fibrils is different in AD and FTDP-17 is consistent with the published findings that tau adopts additional different fibrillar conformations in PiD (Falcon *et al.*, 2018a), CTE (Falcon *et al.*, 2019), and CBD (Zhang *et al.*, 2020) (Figure 5.3). The tau protein seems to be capable of adopting multiple distinct conformations which are disease dependent. This means that the difference in tau structures does not contribute to the variability seen within single

tauopathies. However, the variability in tau structures does contribute to the manifestation of different tauopathies as the conformation of the tau protein has been shown to vary in different diseases. Additionally, the proportion of the different tau fibril conformations may contribute to the variability seen within single tauopathies.

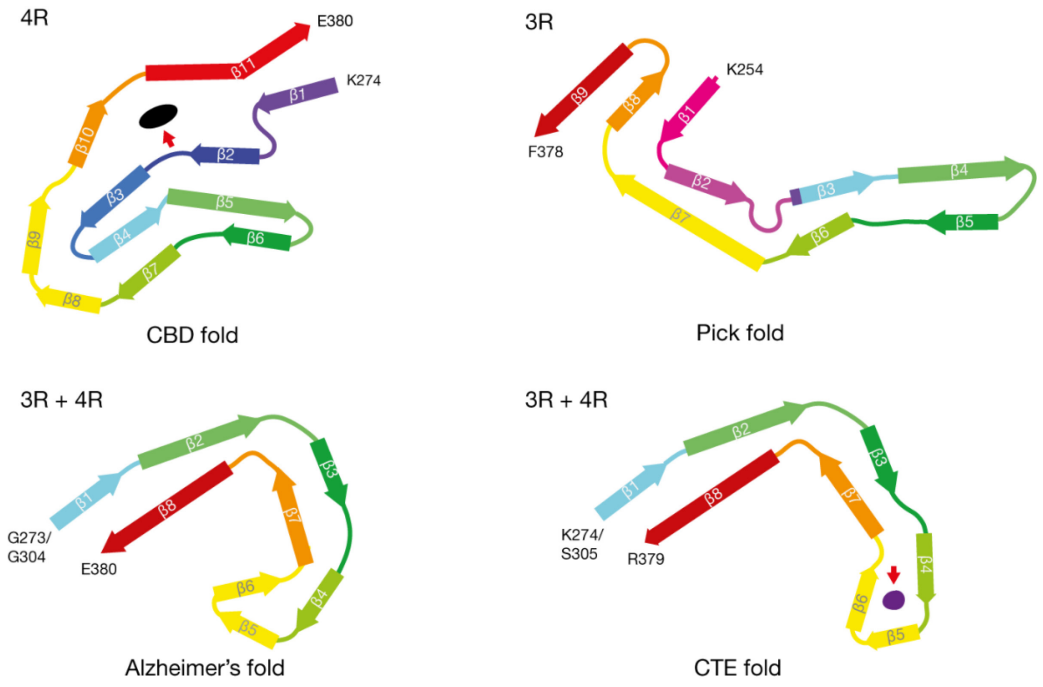

Figure 5.3. Comparison of tau filament cores from CDB, PiD, AD, and CTE. Shown are the schematic structures of the protofilament cores from four tauopathies. In each tauopathy, the tau protein adopts a different structure, demonstrating that the tau protein adopts disease dependent conformations. Red arrows in CBD and CTE folds indicate areas of unknown extra density. This figure was reproduced with permission from Springer Nature Customer Service Centre GmbH: Springer Nature, Nature, Novel tau filament fold in corticobasal degeneration, Wenjuan Zhang *et al.* (2020).

Chapter 6

Conclusion

In conclusion, the major goal of this thesis project was to visualize and reconstruct tau fibrils from human and mouse sources. I have generated 3D-reconstructions of three fibril morphologies, straight, coiled, and twisted ribbon-like, from Tgtau^{P301L} mice, which model human FTDP-17, and of PHFs from human AD. By completing quantitative measurements on electron micrographs of width and helical pitch, I have demonstrated that all the tau fibrils studied here are unique from each other. The 3D-reconstructions I generated of the tau fibrils support this data as they provide visual confirmation of the tau fibril architecture. We can see that the four tau fibril structures; straight fibrils, coiled fibrils, and twisted ribbon-like fibrils from mice, and PHFs from humans; appear different. Additionally, I have provided evidence that AD tau structures remain consistent in different cases, which aligns with published results (Falcon *et al.*, 2018b, Fitzpatrick *et al.*, 2017). The reconstruction of PHFs I generated appears the same as the published structure, and the published tau core structure fits into my 3D-reconstruction. I was not able to confirm the structure of SFs, as the samples which I received did not contain SFs which were candidates for 3D-reconstruction. However, I expect that we would see the same result.

Overall, in this thesis, I demonstrated that the tau protein is capable of adopting numerous different, disease dependent conformations. The structure of the tau fibrils does not vary within a single disease; the structures of PHF from AD remained consistent across all cases I examined and with published tau structures. However, the proportion of the different structures between individual cases does vary. This is seen very clearly in the four Tgtau^{P301L} mouse pathology classes; each class has a different proportion of the three fibril morphologies despite having the same tau mutation. Although additional work is required to confirm, it is likely that the variability in the proportion of different tau fibril morphologies can explain the variability seen in human cases of FTDP-17.

References

1. Arendt T, Stieler JT, Holzer M (2016) Tau and tauopathies. *Brain Research Bulletin* 126: 238-292

2. Aronov S, Aranda G, Behar L, Ginzburg I (2001) Axonal tau mRNA localization coincides with tau protein in living neuronal cells and depends on axonal targeting signal. *J Neurosci* 21: 6577-87

3. Braak H, Alafuzoff I, Arzberger T, Kretzschmar H, Del Tredici K (2006) Staging of Alzheimer disease-associated neurofibrillary pathology using paraffin sections and immunocytochemistry. *Acta neuropathologica* 112: 389-404

4. Brandt R, Leger J, Lee G (1995) Interaction of tau with the neural plasma membrane mediated by tau's amino-terminal projection domain. *J Cell Biol* 131: 1327-40

5. Buee L (2019) Dementia Therapy Targeting Tau. In *Tau Biology*, Takashima A, Wolozin B, Buee L (eds) pp 407-416. Singapore: Springer Singapore

6. Bukar Maina M, Al-Hilaly YK, Serpell LC (2016) Nuclear Tau and Its Potential Role in Alzheimer's Disease. *Biomolecules* 6: 9

7. Caillet-Boudin M-L, Buée L, Sergeant N, Lefebvre B (2015) Regulation of human MAPT gene expression. *Molecular neurodegeneration* 10: 28

8. Chen J, Kanai Y, Cowan NJ, Hirokawa N (1992) Projection domains of MAP2 and tau determine spacings between microtubules in dendrites and axons. *Nature* 360: 674-7

9. Chen Q, Zhou Z, Zhang L, Wang Y, Zhang YW, Zhong M, Xu SC, Chen CH, Li L, Yu ZP (2012) Tau protein is involved in morphological plasticity in hippocampal neurons in response to BDNF. *Neurochem Int* 60: 233-42

10. Corder EH, Saunders AM, Strittmatter WJ, Schmechel DE, Gaskell PC, Small GW, Roses AD, Haines JL, Pericak-Vance MA (1993) Gene dose of apolipoprotein E type 4 allele and the risk of Alzheimer's disease in late onset families. *Science* 261: 921-3

11. Correas I, Padilla R, Avila J (1990) The tubulin-binding sequence of brain microtubule-associated proteins, tau and MAP-2, is also involved in actin binding. *Biochemical Journal* 269: 61-64

12. Daude N, Kim C, Kang S-G, Eskandari-Sedighi G, Haldiman T, Yang J, Fleck SC, Gomez-Cardona E, Han ZZ, Borrego-Ecija S, Wohlgemuth S, Julien O, Wille H, Molina-Porcel L, Gelpi E, Safar JG, Westaway D (2020) Diverse, evolving conformer populations drive distinct phenotypes in

frontotemporal lobar degeneration caused by the same MAPT-P301L mutation. *Acta Neuropathologica*

13. Drewes G, Trinczek B, Illenberger S, Biernat J, Schmitt-Ulms G, Meyer HE, Mandelkow EM, Mandelkow E (1995) Microtubule-associated protein/microtubule affinity-regulating kinase (p110mark). A novel protein kinase that regulates tau-microtubule interactions and dynamic instability by phosphorylation at the Alzheimer-specific site serine 262. *The Journal of biological chemistry* 270: 7679-88

14. Duyckaerts C, Delatour B, Potier M-C (2009) Classification and basic pathology of Alzheimer disease. *Acta Neuropathologica* 118: 5-36

15. Eidenmuller J, Fath T, Maas T, Pool M, Sontag E, Brandt R (2001) Phosphorylation-mimicking glutamate clusters in the proline-rich region are sufficient to simulate the functional deficiencies of hyperphosphorylated tau protein. *Biochem J* 357: 759-67

16. Elie A, Prezel E, Guerin C, Denarier E, Ramirez-Rios S, Serre L, Andrieux A, Fourest-Lieuvin A, Blanchoin L, Arnal I (2015) Tau co-organizes dynamic microtubule and actin networks. *Sci Rep* 5: 9964

17. Erez E, Fass D, Bibi E (2009) How intramembrane proteases bury hydrolytic reactions in the membrane. *Nature* 459: 371

18. Eskandari-Sedighi G, Daude N, Gapeshina H, Sanders DW, Kamali-Jamil R, Yang J, Shi B, Wille H, Ghetti B, Diamond MI, Janus C, Westaway D (2017) The CNS in inbred transgenic models of 4-repeat Tauopathy develops consistent tau seeding capacity yet focal and diverse patterns of protein deposition. *Molecular neurodegeneration* 12: 72

19. Falcon B, Zhang W, Murzin AG, Murshudov G, Garringer HJ, Vidal R, Crowther RA, Ghetti B, Scheres SHW, Goedert M (2018a) Structures of filaments from Pick's disease reveal a novel tau protein fold. *Nature* 561: 137-140

20. Falcon B, Zhang W, Schweighauser M, Murzin AG, Vidal R, Garringer HJ, Ghetti B, Scheres SHW, Goedert M (2018b) Tau filaments from multiple cases of sporadic and inherited Alzheimer's disease adopt a common fold. *Acta Neuropathol*

21. Falcon B, Zivanov J, Zhang W, Murzin AG, Garringer HJ, Vidal R, Crowther RA, Newell KL, Ghetti B, Goedert M, Scheres SHW (2019) Novel tau filament fold in chronic traumatic encephalopathy encloses hydrophobic molecules. *Nature* 568: 420-423

22. Farrer LA, Cupples LA, Haines JL, Hyman B, Kukull WA, Mayeux R, Myers RH, Pericak-Vance MA, Risch N, van Duijn CM (1997) Effects of Age, Sex, and Ethnicity on the Association Between Apolipoprotein E Genotype and Alzheimer Disease: A Meta-analysis. *JAMA* 278: 1349-1356

23. Fitzpatrick AWP, Falcon B, He S, Murzin AG, Murshudov G, Garringer HJ, Crowther RA, Ghetti B, Goedert M, Scheres SHW (2017) Cryo-EM structures of tau filaments from Alzheimer's disease. *Nature* 547: 185-190

24. Frank J, Radermacher M, Penczek P, Zhu J, Li Y, Ladjadj M, Leith A (1996) SPIDER and WEB: processing and visualization of images in 3D electron microscopy and related fields. *J Struct Biol* 116: 190-9

25. Gerson JE, Mudher A, Kayed R (2016) Potential mechanisms and implications for the formation of tau oligomeric strains. *Crit Rev Biochem Mol Biol* 51: 482-496

26. Ghetti B, Oblak AL, Boeve BF, Johnson KA, Dickerson BC, Goedert M (2015) Invited review: Frontotemporal dementia caused by microtubule-associated protein tau gene (MAPT) mutations: a chameleon for neuropathology and neuroimaging. *Neuropathol Appl Neurobiol* 41: 24-46

27. Goate A, Chartier-Harlin M-C, Mullan M, Brown J, Crawford F, Fidani L, Giuffra L, Haynes A, Irving N, James L, Mant R, Newton P, Rooke K, Roques P, Talbot C, Pericak-Vance M, Roses A, Williamson R, Rossor M, Owen M et al. (1991) Segregation of a missense mutation in the amyloid precursor protein gene with familial Alzheimer's disease. *Nature* 349: 704-706

28. Goedert M, Spillantini MG, Jakes R, Rutherford D, Crowther RA (1989a) Multiple isoforms of human microtubule-associated protein tau: sequences and localization in neurofibrillary tangles of Alzheimer's disease. *Neuron* 3: 519-526

29. Goedert M, Spillantini MG, Potier MC, Ulrich J, Crowther RA (1989b) Cloning and sequencing of the cDNA encoding an isoform of microtubule-associated protein tau containing four tandem repeats: differential expression of tau protein mRNAs in human brain. *The EMBO Journal* 8: 393-399

30. Goode BL, Denis PE, Panda D, Radeke MJ, Miller HP, Wilson L, Feinstein SC (1997) Functional interactions between the proline-rich and repeat regions of tau enhance microtubule binding and assembly. *Mol Biol Cell* 8: 353-65

31. Götz J, Chen F, Barmettler R, Nitsch RM (2001) Tau Filament Formation in Transgenic Mice Expressing P301L Tau. *Journal of Biological Chemistry* 276: 529-534

32. Guo T, Noble W, Hanger DP (2017) Roles of tau protein in health and disease. *Acta Neuropathologica* 133: 665-704

33. Hanger DP, Anderton BH, Noble W (2009) Tau phosphorylation: the therapeutic challenge for neurodegenerative disease. *Trends in Molecular Medicine* 15: 112-119

34. Hardy J, Higgins G (1992) Alzheimer's disease: the amyloid cascade hypothesis. *Science* 256: 184-185

35. Harold D, Abraham R, Hollingworth P, Sims R, Gerrish A, Hamshere ML, Pahwa JS, Moskvina V, Dowzell K, Williams A, Jones N, Thomas C, Stretton A, Morgan AR, Lovestone S, Powell J, Proitsi P, Lupton MK, Brayne C, Rubinsztein DC et al. (2009) Genome-wide association study identifies variants at CLU and PICALM associated with Alzheimer's disease. *Nat Genet* 41: 1088-93

36. Harris JR (2015) Transmission electron microscopy in molecular structural biology: A historical survey. *Archives of Biochemistry and Biophysics* 581: 3-18

37. He HJ, Wang XS, Pan R, Wang DL, Liu MN, He RQ (2009) The proline-rich domain of tau plays a role in interactions with actin. *BMC Cell Biol* 10: 81

38. Hoover BR, Reed MN, Su J, Penrod RD, Kotilinek LA, Grant MK, Pitstick R, Carlson GA, Lanier LM, Yuan LL, Ashe KH, Liao D (2010) Tau mislocalization to dendritic spines mediates synaptic dysfunction independently of neurodegeneration. *Neuron* 68: 1067-81

39. Hutton M, Lendon CL, Rizzu P, Baker M, Froelich S, Houlden H, Pickering-Brown S, Chakraverty S, Isaacs A, Grover A, Hackett J, Adamson J, Lincoln S, Dickson D, Davies P, Petersen RC, Stevens M, de Graaff E, Wauters E, van Baren J et al. (1998) Association of missense and 5′-splice-site mutations in tau with the inherited dementia FTDP-17. *Nature* 393: 702-705

40. Jeganathan S, von Bergen M, Brutlach H, Steinhoff HJ, Mandelkow E (2006) Global hairpin folding of tau in solution. *Biochemistry* 45: 2283-93

41. Jeganathan S, von Bergen M, Mandelkow EM, Mandelkow E (2008) The natively unfolded character of tau and its aggregation to Alzheimer-like paired helical filaments. *Biochemistry* 47: 10526-39

42. Jenkins SM, Johnson GV (1998) Tau complexes with phospholipase C-gamma in situ. *Neuroreport* 9: 67-71

43. Kelleher RJ, 3rd, Shen J (2017) Presenilin-1 mutations and Alzheimer's disease. *Proceedings of the National Academy of Sciences of the United States of America* 114: 629-631

44. Konzack S, Thies E, Marx A, Mandelkow EM, Mandelkow E (2007) Swimming against the tide: mobility of the microtubule-associated protein tau in neurons. *J Neurosci* 27: 9916-27

45. Kopke E, Tung YC, Shaikh S, Alonso AC, Iqbal K, Grundke-Iqbal I (1993) Microtubule-associated protein tau. Abnormal phosphorylation of a non-paired helical filament pool in Alzheimer disease. *The Journal of biological chemistry* 268: 24374-84

46. Kovacs GG (2016) Molecular Pathological Classification of Neurodegenerative Diseases: Turning towards Precision Medicine. *International Journal of Molecular Sciences* 17: 189

47. Ksiezak-Reding H, Pyo HK, Feinstein B, Pasinetti GM (2003) Akt/PKB kinase phosphorylates separately Thr212 and Ser214 of tau protein in vitro. *Biochim Biophys Acta* 1639: 159-68

48. Lee G, Cowan N, Kirschner M (1988) The primary structure and heterogeneity of tau protein from mouse brain. *Science* 239: 285-8

49. Lee G, Newman ST, Gard DL, Band H, Panchamoorthy G (1998) Tau interacts with src-family non-receptor tyrosine kinases. *Journal of Cell Science* 111: 3167-3177

50. Li X, Kumar Y, Zempel H, Mandelkow EM, Biernat J, Mandelkow E (2011) Novel diffusion barrier for axonal retention of Tau in neurons and its failure in neurodegeneration. *Embo j* 30: 4825-37

51. Li XC, Hu Y, Wang ZH, Luo Y, Zhang Y, Liu XP, Feng Q, Wang Q, Ye K, Liu GP, Wang JZ (2016) Human wild-type full-length tau accumulation disrupts mitochondrial dynamics and the functions via increasing mitofusins. *Sci Rep* 6: 24756

52. Liu C-C, Kanekiyo T, Xu H, Bu G (2013a) Apolipoprotein E and Alzheimer disease: risk, mechanisms and therapy. *Nature Reviews Neurology* 9: 106-118

53. Liu C, Gotz J (2013b) Profiling murine tau with 0N, 1N and 2N isoform-specific antibodies in brain and peripheral organs reveals distinct subcellular localization, with the 1N isoform being enriched in the nucleus. *PLoS One* 8: e84849

54. Liu C, Song X, Nisbet R, Gotz J (2016) Co-immunoprecipitation with Tau Isoform-specific Antibodies Reveals Distinct Protein Interactions and Highlights a Putative Role for 2N Tau in Disease. *The Journal of biological chemistry* 291: 8173-88

55. Liu F, Li B, Tung EJ, Grundke-Iqbal I, Iqbal K, Gong CX (2007) Site-specific effects of tau phosphorylation on its microtubule assembly activity and self-aggregation. *Eur J Neurosci* 26: 3429-36

56. Ludtke SJ, Baldwin PR, Chiu W (1999) EMAN: Semiautomated Software for High-Resolution Single-Particle Reconstructions. *Journal of Structural Biology* 128: 82-97

57. Magnani E, Fan J, Gasparini L, Golding M, Williams M, Schiavo G, Goedert M, Amos LA, Spillantini MG (2007) Interaction of tau protein with the dynactin complex. *Embo j* 26: 4546-54

58. Mahley RW, Stanley C. Rall J (2000) Apolipoprotein E: Far More Than a Lipid Transport Protein. *Annual Review of Genomics and Human Genetics* 1: 507-537

59. Mandelkow E-M, Mandelkow E (2012) Biochemistry and Cell Biology of Tau Protein in Neurofibrillary Degeneration. *Cold Spring Harbor Perspectives in Medicine* 2

60. Mukrasch MD, von Bergen M, Biernat J, Fischer D, Griesinger C, Mandelkow E, Zweckstetter M (2007) The "jaws" of the tau-microtubule interaction. *The Journal of biological chemistry* 282: 12230-9

61. Muller R, Heinrich M, Heck S, Blohm D, Richter-Landsberg C (1997) Expression of microtubule-associated proteins MAP2 and tau in cultured rat brain oligodendrocytes. *Cell Tissue Res* 288: 239-49

62. Noble M, Lewis SA, Cowan NJ (1989) The microtubule binding domain of microtubule-associated protein MAP1B contains a repeated sequence motif unrelated to that of MAP2 and tau. *Journal of Cell Biology* 109: 3367-3376

63. Papasozomenos SC, Binder LI (1987) Phosphorylation determines two distinct species of Tau in the central nervous system. *Cell Motil Cytoskeleton* 8: 210-26

64. Pettersen EF, Goddard TD, Huang CC, Couch GS, Greenblatt DM, Meng EC, Ferrin TE (2004) UCSF Chimera--a visualization system for exploratory research and analysis. *J Comput Chem* 25: 1605-12

65. Qi H, Cantrelle FX, Benhelli-Mokrani H, Smet-Nocca C, Buee L, Lippens G, Bonnefoy E, Galas MC, Landrieu I (2015) Nuclear magnetic resonance spectroscopy characterization of interaction of Tau with DNA and its regulation by phosphorylation. *Biochemistry* 54: 1525-33

66. Reynolds CH, Garwood CJ, Wray S, Price C, Kellie S, Perera T, Zvelebil M, Yang A, Sheppard PW, Varndell IM, Hanger DP, Anderton BH (2008) Phosphorylation regulates tau interactions with Src homology 3 domains of phosphatidylinositol 3-kinase, phospholipase Cgamma1, Grb2, and Src family kinases. *The Journal of biological chemistry* 283: 18177-86

67. Safar J, Wille H, Itri V, Groth D, Serban H, Torchia M, Cohen FE, Prusiner SB (1998) Eight prion strains have PrPSc molecules with different conformations. *Nature Medicine* 4: 1157-1165

68. Sahara N, DeTure M, Ren Y, Ebrahim A-S, Kang D, Knight J, Volbracht C, Pedersen JT, Dickson DW, Yen S-H, Lewis J (2013) Characteristics of TBS-extractable hyperphosphorylated tau species: Aggregation intermediates in rTg4510 mouse brain. *Journal of Alzheimer's disease : JAD* 33: 249-263

69. Sanders David W, Kaufman Sarah K, DeVos Sarah L, Sharma Apurwa M, Mirbaha H, Li A, Barker Scarlett J, Foley Alex C, Thorpe Julian R, Serpell Louise C, Miller Timothy M, Grinberg Lea T, Seeley William W, Diamond Marc I (2014) Distinct Tau Prion Strains Propagate in Cells and Mice and Define Different Tauopathies. *Neuron* 82: 1271-1288

70. Seidler PM, Boyer DR, Rodriguez JA, Sawaya MR, Cascio D, Murray K, Gonen T, Eisenberg DS (2018) Structure-based inhibitors of tau aggregation. *Nature chemistry* 10: 170-176

71. Sengupta A, Kabat J, Novak M, Wu Q, Grundke-Iqbal I, Iqbal K (1998) Phosphorylation of tau at both Thr 231 and Ser 262 is required for maximal inhibition of its binding to microtubules. *Arch Biochem Biophys* 357: 299-309

72. Spillantini MG, Crowther RA, Kamphorst W, Heutink P, van Swieten JC (1998) Tau Pathology in Two Dutch Families with Mutations in the Microtubule-Binding Region of Tau. *The American Journal of Pathology* 153: 1359-1363

73. Tashiro K, Hasegawa M, Ihara Y, Iwatsubo T (1997) Somatodendritic localization of phosphorylated tau in neonatal and adult rat cerebral cortex. *Neuroreport* 8: 2797-801

74. Thinakaran G (1999) The role of presenilins in Alzheimer's disease. *J Clin Invest* 104: 1321-1327

75. Tomita T, Maruyama K, Saido TC, Kume H, Shinozaki K, Tokuhiro S, Capell A, Walter J, Grunberg J, Haass C, Iwatsubo T, Obata K (1997) The presenilin 2 mutation (N141I) linked to familial Alzheimer disease (Volga German families) increases the secretion of amyloid beta protein ending at the 42nd (or 43rd) residue. *Proceedings of the National Academy of Sciences of the United States of America* 94: 2025-30

76. Trojanowski JQ, Schuck T, Schmidt ML, Lee VM (1989) Distribution of tau proteins in the normal human central and peripheral nervous system. *J Histochem Cytochem* 37: 209-15

77. van Heel M, Harauz G, Orlova EV, Schmidt R, Schatz M (1996) A new generation of the IMAGIC image processing system. *J Struct Biol* 116: 17-24

78. Vanderweyde T, Apicco DJ, Youmans-Kidder K, Ash PEA, Cook C, Lummertz da Rocha E, Jansen-West K, Frame AA, Citro A, Leszyk JD, Ivanov P, Abisambra JF, Steffen M, Li H, Petrucelli L, Wolozin B (2016) Interaction of tau with the RNA-Binding Protein TIA1 Regulates tau Pathophysiology and Toxicity. *Cell Rep* 15: 1455-1466

79. Wang X, Wang D, Zhao J, Qu M, Zhou X, He H, He R (2006) The proline-rich domain and the microtubule binding domain of protein tau acting as RNA binding domains. *Protein Pept Lett* 13: 679-85

80. Williams DB, Carter CB (1996) The Instrument. In *Transmission Electron Microscopy: A Textbook for Materials Science*, pp 131-153. Boston, MA: Springer US

81. Wszolek ZK, Tsuboi Y, Ghetti B, Pickering-Brown S, Baba Y, Cheshire WP (2006) Frontotemporal dementia and parkinsonism linked to chromosome 17 (FTDP-17). *Orphanet Journal of Rare Diseases* 1: 30-30

82. Zhang W, Tarutani A, Newell KL, Murzin AG, Matsubara T, Falcon B, Vidal R, Garringer HJ, Shi Y, Ikeuchi T, Murayama S, Ghetti B, Hasegawa M, Goedert M, Scheres SHW (2020) Novel tau filament fold in corticobasal degeneration. *Nature*